UCLouvain

École polytechnique de Louvain

High-Entropy Nitrides of Late Transition Metals

Author : **Maryam Tahir**
Supervisors : **PD Dr Emanuel Ionescu**, **Prof. Dr Gian-Marco Rignanese**
Readers : **Prof. Dr Pascal Jacques**
Academic year 2020–2021
Master [120] in Chemical and Materials Engineering

Abstract

High-entropy ceramics (HEC) are an interesting class of high-entropy materials, showing remarkable properties, allowing flexible ways to obtain a combination of properties in a single material which has application in diverse fields. Synthesis of stable high entropy oxides was achieved in 2015 and other classes were synthesized right after. A promising class of HECs that have gained attention recently is high-entropy nitrides (HEN). As with high-entropy alloys (HEA), the primary challenge is the synthesis of stable high entropy single-phase materials. In this work, some recent HECs are discussed along with the synthesis procedures and novel applications. Furthermore, new synthesis routes are investigated for the formation of a high-entropy nitride constituting late transition metals.

Acknowledgement

I am grateful to my supervisor **Dr. rer. Nat. Emanuel Ionescu** from TU Darmstadt for his constant support and guidance during the course of the work. I am thankful to my supervisor **Prof. Dr. Gian-Marco Rignanese** from UCLouvain for enabling me to perform this work, and to **Prof. Dr. Pascal Jacques** for his valuable input being a part of the jury for evaluation of the thesis. I would also like to thank Prof. Dr. Ralph Riedel, for allowing me to carry out my work in Fachgebiet Disperse Feststoffe (Dispersive Solids research group), Material Science Department, TU Darmstadt. I would like to pay my regards to **Dr. Marc Widenmeyer** (Materials and Resources, TU Darmstadt) for providing with thermo-gravimetric analysis, and for his valuable guidance. I am grateful to my friend **Emre Güneş** (Master Student at Materials and Resources, TU Darmstadt) for his support with XRD measurements. I would like to thank **Jan Bernauer** for his guidance and support in the labs, and all my friends and colleagues from Dispersive Solids group for their support. I am grateful to my friend **Osama Akhter** for valuable input in reviewing and structuring the documentation this work. Lastly, I would like to acknowledge the moral support of my parents throughout my studies.

Table of Contents

List of Figures

List of Tables

1. Introduction

The technology of ceramics has existed since ancient times. Evolution of this technology has been a subject of great interest for materials scientists and engineers. Presently, a wide variety of ceramic class of materials exist, and they are employed in daily-life technologies such as clay products, abrasives, enamels etc., as well as advanced categories such as dielectrics, ferroelectrics, semi-conductors, ceramic matrix composites, ceramic fibers etc. The research on optimizing already exiting synthesis and processing techniques, and also novel approaches for new and advanced materials is ever-growing and serves as a road to commercialization of new technologies.

One of such recent emerging topics has been High Entropy Ceramics (HECs), derived from the concept of High Entropy Alloys (HEAs). This field of study first surfaced in 2004, and has recently been under focus, employing the concepts of entropy of mixing, and entropy of configuration of materials [1].

HECs have exhibited exciting potential as candidates for important applications such as energy sector, functional, and high-temperature performance etc. For instance, the system $(MgCoNiCuZn)O$ has been reported to be capable of superionic conductivity, making it a good candidate as anode material in Lithium-ion batteries [2]. Another interesting capability of HECs is the thermochemical water-splitting, and catalysis which can lead way to advancement in clean energy storage technologies [3]. Furthermore, HECs, particularly high-entropy nitrides, have remarkable hardness and toughness and have immense potential for applications requiring thermal and environmental protection [4, 5]. The very low thermal conductivity makes HECs capable candidates as thermoelectric materials. [6]

The system of multicomponent cantor alloys is a well-known combination [7] and high-entropy oxides of this compositional system have also gained a lot of attention recently [8]. In this work, an attempt to synthesize high-entropy nitride of this compositional class has been done, utilizing novel synthesis approaches, which are easily accessible and energy-efficient.

Two material systems have been worked on, in order to analyze the effect of the synthesis route on the final ceramic product. Binary Fe2N system was investigated in order to evaluate whether the approach is suitable for obtaining nitrides or not. The results of this system showed promising potential for synthesis of nitrides. The other system targeted was five-component high-entropy nitride of Cobalt, Chromium, Manganese, Iron, and Nickel.

2. Fundamentals

Alloying has been used as a means for modifying properties of materials since early times. Conventional alloying has consisted of inducing minute quantities of allying elements to a base element. Through this traditional approach, not many elemental combinations are possible. Hence, the concept of high entropy alloys is quite interesting. As opposed to the conventional alloying concept, this approach involves mixing of several elements in equal ratios, or considerably higher amounts. Hence, high entropy materials have recently gained significant attention. A lot of work is being done on high entropic alloys.

In this section, the fundamental concepts related to high-entropy alloys is briefly touched upon based on the current advancements. Furthermore, High Entropy Ceramics (HECs) have also been introduced, and the current synthesis approaches and advancements have been reviewed. The section concludes with the current and possible future prospects of HEAs and HECs.

2.1. High-Entropy Alloys

The alloying mechanism involves mixing of the component elements, which can result in either a solid solution, or intermetallic phases, depending on the relative Gibbs free energies of the phases [9].

If A and B are two components of a binary alloy,

$$A + B = AB\ (solid\ solution)\colon \Delta G_{mix} = \Delta H_{mix} - T\Delta S_{mix} \quad (1)$$

$$A + B = AB\ (intermetallic\ phase)\colon \Delta G_f = \Delta H_f - T\Delta S_f \quad (2)$$

Where

$\Delta G_{mix} =$ Gibbs Free Energy of mixing,
$\Delta S_{mix} =$ Entropy of mixing,
$\Delta H_{mix} =$ Enthalpy of mixing,

and,

$\Delta G_f =$ Gibbs Free Energy of formation of intermetallic phase AB,
$\Delta S_f =$ Entropy of formation of intermetallic phase AB,
$\Delta H_f =$ Enthalpy of formation of intermetallic phase AB, and
$T =$ Absolute Temperature.

For intermetallic phases other than composition AB, equations similar to equation (1) and (2), are necessary for every composition. If the Gibbs free energy of mixing is lower than that of formation of intermetallic compound, solid solution will be formed, and vice versa. However, it can also be possible that several solid solutions with different compositions or structures form, instead of one [9]. Furthermore, the entire formation of intermetallic phase is also not definite. It is also likely that precipitates of intermetallic phases nucleate in certain regions which have higher concentrations of either of the component. In such a situation, the free energy would correspond to the sum of ΔG_{mix} and ΔG_f. If the number of constituent elements increase, the complexity of the system increases. This is because the possibility and number of coexisting phases increases, as per the Gibbs phase rule [9].

For such multicomponent systems, each possible phase has a range of composition where it is stable. For multicomponent phases, energy for formation of defects that make up for stoichiometric deviations, need

to be compensated for. Hence, the increase in components leads to more complexity. Figure 2-1 shows the probable transformations that could occur in a ternary system.

These complications in multicomponent systems had been a discouragement for researchers to pursue this field. However, it was JW Yeh in Taiwan, who proposed that materials be categorized based on configurational entropy. He suggested the term "high-entropy alloys" for alloys with five constituent elements at minimum, with the content of each component being greater than 5 atomic percent, and the configurational entropy be above 1.62R or 1.5R, where R refers to ideal gas constant [1].

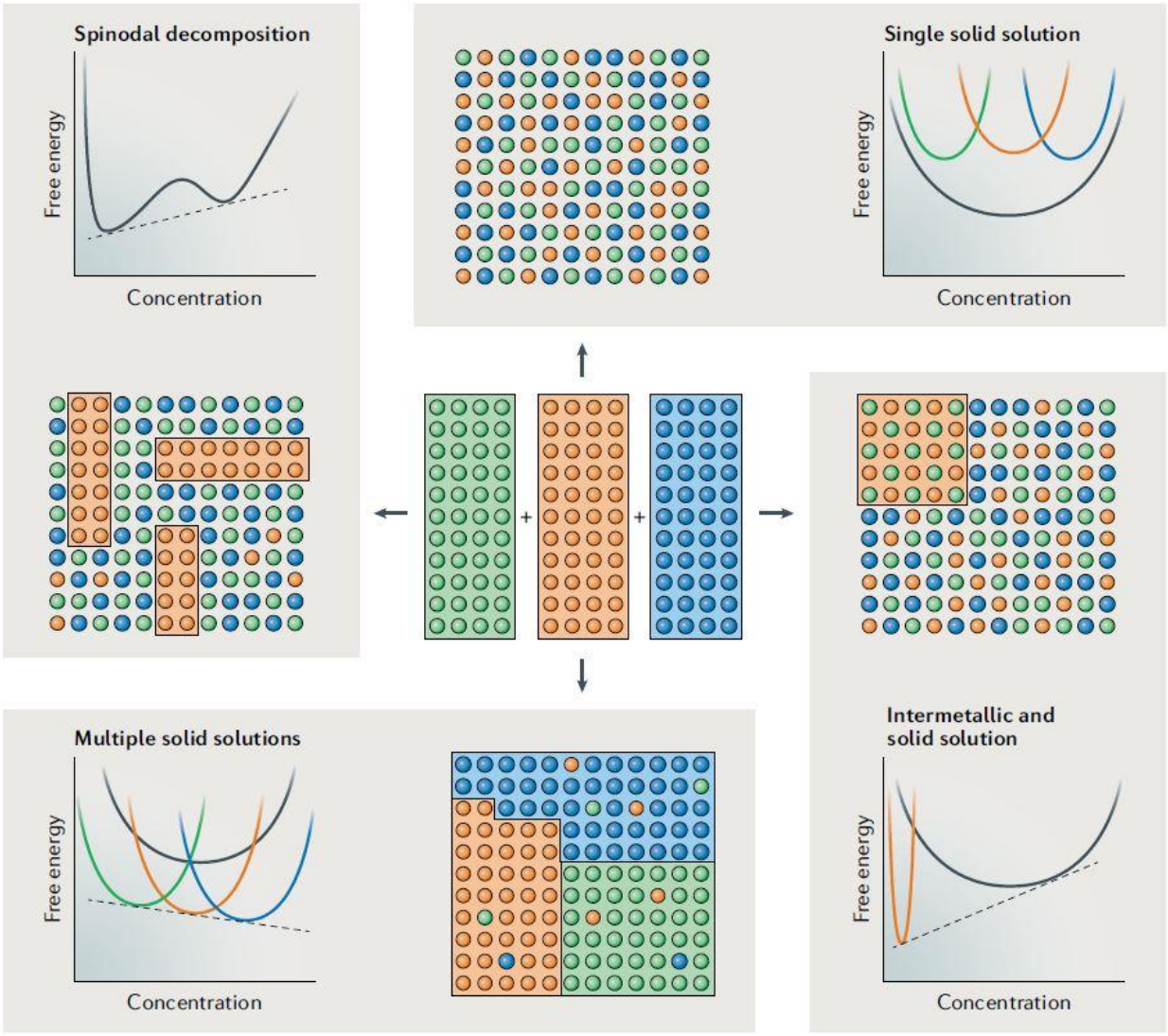

Figure 2-1 Possible transformations in a ternary system with corresponding free energy plots [9].

Yeh et. al considered an ideal solid solution and ordered intermetallic, in which case, the stability of solid solution versus the intermetallic would only depend on $-T\Delta S_{mix}$ and ΔH_f [10]. The ideal entropy of mixing is,

$$\Delta S_{mix} = -R \sum x_i \ln x_i \tag{3}$$

Where

R = Ideal gas constant,
x_i = mole fraction of i^{th} component.

In case of high entropy alloys, the ratios of constituent elements are equiatomic, and hence,

$$\Delta S_{mix} = R \ln n \quad (4)$$

Where n is the number of constituent elements. If n is 4, ΔS_{mix} is $1.39R$. For $n = 5$, it is $1.61R$ and $1.79R$ for 6 elements system.

The alloys are hence also classified on the basis of entropy. This classification stems from the entropy-based definition of HEAs, i.e., the maximization the entropy of mixing in order to make the solid-solutions stable.

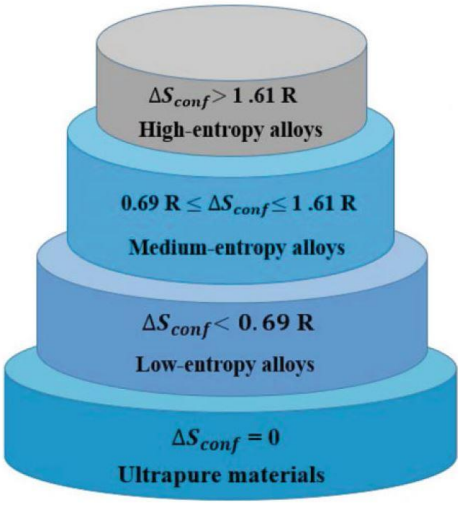

Figure 2-2 Entropy-based classification of materials [11].

However, as the research on this class of materials continue, it is understood better that the stability of HEAs is not entirely dependent on entropy measures. Recent developments have also attempted to define stability criteria, taking into account, other factors such as the ΔH_{mix} term, and the criteria defined by the Hume-Rothery rules for the stability of the solid solution. Hume-Rothery or H-R rules define the criteria for alloy formation in terms of the difference in atomic diameters of the constituent elements, the crystal structures, electronegativity difference, and electron concentration ratio of the alloy [12].

Furthermore, if the aim is to obtain phase-pure alloy, it is of significance to consider high-temperature stability of the alloys as well, as the advanced applications require high-performance materials to be used at elevated temperature. One way to do so would be the application of thermodynamic models to compute phase diagrams in order to predict stability conditions for the alloy [13, 14].

2.1.1. Main characteristics of High Entropy Alloys

HEA systems are very interesting, as they have certain characteristics that distinguish them from conventional alloys. These characteristics are responsible for the superior mechanical properties of the HEAs [15]. Thermodynamics aspect: High-Entropy effect

As suggested by the name of the class of alloys, this feature of HEAs is of high significance. As explained in the previous section, this effect gives way to stability of solid solution by an increasing the number of component elements, resulting in a high entropy of mixing, and consequently decreasing the free energy for mixing.

2.1.1.1. Kinetics aspect: Sluggish diffusion effect

Tsai et al. studied the sluggish diffusion in the $CoCrFeMnNi$ high entropy alloy, and it was concluded that in HEAs, the self-diffusion coefficient of constituent elements is significantly lower as compared to traditional alloys. This is because the diffusion mechanism in HEAs occur by through occupation of vacancies. The melting points and bond energies are different for atoms, the atom with higher mobility is likely to fill the vacancy. After the occupation of vacancy, if the energy decreases, the atom would not easily escape the vacancy, and hence the diffusion would be hindered [16]. The lattice distortion also affects the diffusion rate of atoms in the HEA. This effect can give way to superior desirable properties like creep resistance in the material [17].

2.1.1.2. Structural aspect: Severe Lattice distortion

In equimolar HEAs, the solute atoms have varying atomic sizes, which causes severe lattice distortion. Larger atoms push against neighboring atoms, and smaller atoms are surrounded by free volume. This causes the lattice to be highly strained and as a result, total free energy of the HEA increases. This effect can have a notable impact on the properties of the HEA, such as increase of hardness due to solid solution-hardening mechanism. Lattice distortion also impacts thermal conductivity and x-ray diffuse scattering [17, 18].

2.1.1.3. Cocktail effect

The cocktail effect, first coined by Ranganatha [19], refers to the interaction between different constituent elements of the high-entropy alloy, giving rise to a composite effect. Through the utilization of this effect, the alloy systems can have a wider range, and minute elemental additions can be made to enhance the properties and modify the microstructure. For instance, in a work of Tong et al., different fractions of Aluminum were added to the 5-component system $CoCrCuFeNi$ to enhance hardness of the material and result in different phases [20].

2.1.2. Important High-Entropy Alloy systems

Presently, HEAs are categorized as 1st generation and 2nd generation, based on the timeline of their discovery, as well as their phase composition. The entropy-based definition of alloys is the basis of the 1st generation HEAs, that are solid solutions having 5 or more components in equal concentration. Recent advancements have lifted the restrictions that were imposed on HEAs because of the entropy-based definition. The 2nd generation comprises HEAs having four or more elements and are multiphasic. However, the 1st generation alloys are more relevant to the focus of this work. Till now, FCC, BCC, HCP, and orthorhombic structures have been investigated [9]. Some of these systems have been discussed below.

2.1.2.1. FCC $CrMnFeCoNi$ Alloy

This system is one of the earliest FCC structured HEAs to have been synthesized and has been the most investigated HEA. This system is named Cantor alloy, after the name of the researcher that worked on the system. Cantor initiated his investigation regarding multicomponent systems in 1981 and discovered that $Co_{20}Cr_{20}Fe_{20}Mn_{20}Ni_{20}$ is capable of having one phase, i.e., FCC dendritic structure [21]. The properties

of this system have only been investigated recently. It has some unique characteristics, that are different from conventional FCC metallic structures. Although the yield strength of the alloy has been reported to change with temperature, but strain-rate and strength do not exhibit significant dependency on temperature [15]. Initial researches have indicated the cause to be high work-hardenability of the HEA, that could have a link to nano-twins due to deformation. These defects are likely to improve resistance of material to necking [22].

Hence, this class of materials is remarkably damage resistant and suitable for use as high-performance construction materials. Cantor alloy has a random distribution of constituent elements, and there is no order.

Figure 2-3 shows fracture toughness vs yield strength diagram of different classes of materials. It shows the Cantor alloy and its derivative $CrCoNi$ alloy to be on the top-right position of the plot, having rather high fracture toughness, but not very high yield strength. The trend observed in BCC structure is the opposite, they usually have very high yield strength [22].

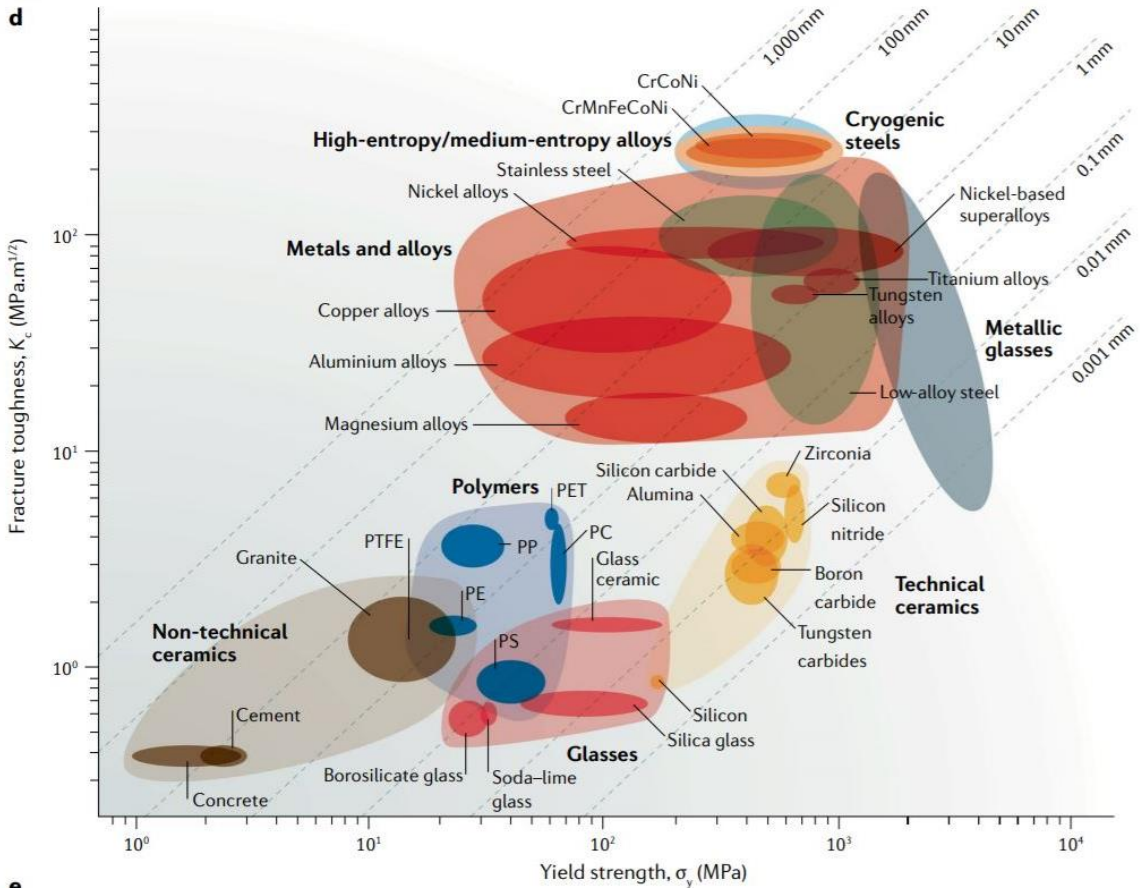

Figure 2-3 Ashby plot of strength versus fracture toughness [9].

2.1.2.2. BCC $TiZrHfNbTa$ Alloy

Being among the first and a hot topic since their invention in 2004, FCC Cantor alloy and its derivates have undergone thorough research. But the same cannot be said about BCC HEAs. This is largely because of

their very high melting points and brittleness, complicating removing cast defects or modify their microstructures to achieve microstructure stability and homogeneity. [23]. However, following Oleg Senkov's success at synthesis of the BCC Senkov alloy $TiZrHfNbTa$ in 2015, BCC HEAs have garnered interest, particularly for their potential as refractory HEAs. This has led to BCC HEAs being commonly referred to as Refractory HEAs.

Senkov found initial success in the synthesis of equiatomic BCC $TiZrHfNbTa$ (Senkov) HEA in 2011 using arc melting. After hot isostatic pressing, it exhibited a dendritic microstructure 72. The Senkov Alloy has exhibited ductility at room temperature while several of its derivatives have also shown adequate low temperature ductility [24, 25].

The BCC Senkov HEA has also demonstrated metastability at intermediate temperatures, similar to the FCC Cantor allow. Senkov et al. successfully cold rolled the BCC $TiZrHfNbTa$ alloy into a thin sheet, followed by annealing at $800°C$, $1000°C$, and $1200°C$. The $800°C$ sample resulted in two BCC phases and were notably more brittle compared to the samples annealed at $1000°C$ and $1200°C$, both of which resulted in a single BCC phase [23]. While metastable structures find their applications in low temperature systems, long-term kinetic stability can be questionable.

2.1.3. Applications of High Entropy Alloys

2nd generation HEAs have significant potential as superalloys, for applications for performance under harsh conditions, such as turbine blades, nuclear reactors, aerospace materials, oil and gas industries etc. [5] A recent development is the novel non-equimolar $Al_xCo_{1.5}CrFeNi_{1.5}\,Ti_{0.5-x}$ alloy systems having γ FCC matrix with $L1_2$ γ' precipitates as the dispersive phase. [26]. The synthesis of these materials is carried out based on the HEA, hence, the term High-Entropy Superalloys (HESA) has been used to refer to these systems [26].

HEAs also have the potential to exceed the high-temperature capabilities of conventional superalloys, such HEAs are referred to as high-entropy refractory alloys. Initially, BCC $MoNbTaW$ and $MoNbTaVW$ refractory HEAs were reported and found to have retained yield strengths of 405 and 477 MPa at $1600°C$, respectively. [23] Later, Senkov alloys were also synthesized and investigated. [27]

Because suitable alloy design of HEAs has been proven to give promising properties, such as high hardness, softening resistance at high temperature, wear resistance, and corrosion resistance, some of them have been identified as good candidates for binders in cemented carbides and cements to improve properties and reduce cost. Among these candidates, $Al_{0.5}CoCrCuFeNi$ HEA with an FCC structure has recently been reported to be a promising binder for wetting tungsten carbide and hindering its coarsening [28]

HEAs have also been reported to have potential as protective hard coatings, due to their excellent mechanical and wear-resistant properties. [5] HEAs are also relevant for diffusion barrier applications. [5] HEAs also offer advancements in applications such as irradiation-resistant materials for nuclear reactors. HEAs have been reported to also have high stresses at atomic scale due to the solid solution of elements with different sizes. [29] Due to these stresses, amorphization occurs in HEAs when they are irradiated. The thermal spikes cause localized melting and recrystallization, leading to lesser defects in HEAs, in comparison with traditional alloys, making them suitable for use in nuclear facilities [30].

2.2. High-Entropy Ceramics

Ceramics are a diverse class of inorganic, non-metallic materials made up of metallic and/or non-metallic components, known for their desirable properties such as thermal, electrical and corrosion resistance, hardness, and strength [31]. The term *ceramic* comes from the Greek word *κεραμικός* (*keramikos*), derived from *κέραμος* (*keramos*), which means "pottery clay". In some publications, the word *κεραμικός* (*keramikos*) is also translated as "burnt stuff", which is noted to indicate the heat treatment processes often involved in the synthesis of ceramics [31].

While humans have been making and working with ceramics for at least 26,000 years [32], until recently, this class of materials comprised of what is now referred to as traditional ceramics. This is a very diverse class of materials including clay products (e.g., earthenware, stoneware, porcelain), refractories, glasses, abrasives, cements and so on [31], with a wide range of applications such as pottery, sculpting, construction, thermal and electrical insulation, vision correction and so on.

Over the last century or so, however, thanks to advancement in large-scale synthesis techniques, a new generation of ceramics, often termed as advanced ceramics, has been developed [33]. This new class of materials has seen rapid advancements in terms of material design and synthesis, offering an even wider range of properties and applications and allowing us to develop materials with very desirable combination of properties and leading to greater and greater advances in technology [34]. The applications of these advanced ceramics materials include automotive, semiconductors, microfabrication [35], electronics, optical fibers, medicine and implants, engineering, industrial manufacturing and processing, and even space technology.

The chemical bonds in ceramics can be covalent, ionic, or polar covalent, depending on the composition. Ionic ceramics are typically composed of a metal and a non-metal part while ceramics that are formed between a metalloid and a non-metal part are primarily covalent. Save for glasses, which are amorphous solids, most ceramics observe a highly crystalline structure [36].

High-Entropy Ceramics, or HECs, are a novel class of ceramics with at least four different cations or anions. They are based on the entropy-stabilized single-phase concept developed by Yeh et al. in 2004 for HEAs [10]. As such, they share similarities with HEAs in terms of contribution of high configurational entropy to their formation as well as some properties. However, being a fundamentally different class of materials, they have structurally different from HEAs, offering significantly different properties and applications [37]. Furthermore, HECs offer better structural diversity as well as a huge potential for property tuning through band tuning and phonon engineering [10, 37]. As of this report, synthesis of HECs in at least eight different crystal structures has been published and are illustrated in Figure 2-4 .

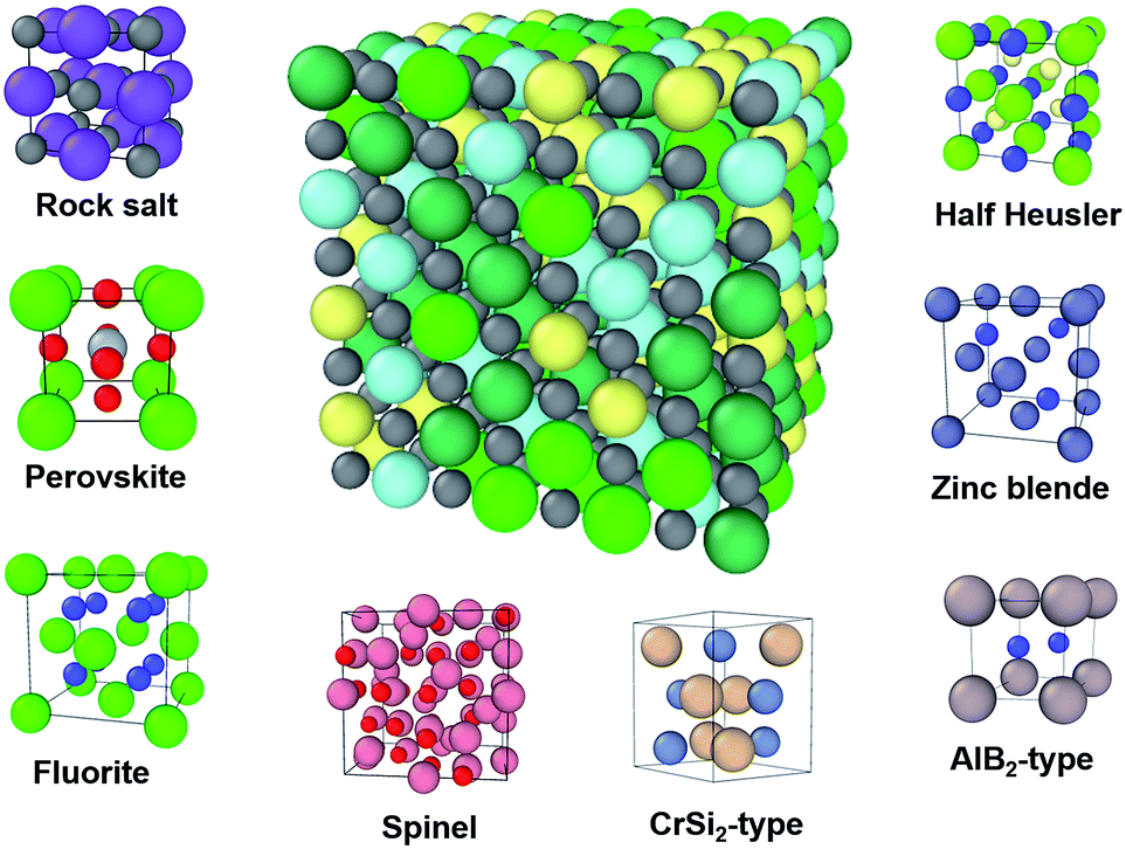

Figure 2-4 Crystal structure diversity of the HEC family, based on successfully fabricated HECs. The central image depicts a supercell of a rock salt HEC with anions in dark grey and randomly distributed cations [37].

Similar to HEAs, the prediction of accessible stable-phase HECs is a topic of great importance. Thermodynamically, Gibbs free energy can be used to determine the phase stability of HECs. Analogous to HEAs, the Gibbs free energy for HECs is defined as

$$\Delta G_{mix} = \Delta H_{mix} - T\Delta S_{mix} \tag{5}$$

Where

ΔG_{mix} = Gibbs Free Energy of mixing,
ΔH_{mix} = Enthalpy of mixing, and
ΔS_{mix} = Entropy of mixing, which can be expressed as

$$\Delta S_{conf} = -R \sum_{x_i} \left(x_i \sum_{n} c_j \ln c_j \right) \tag{6}$$

Where

ΔS_{conf} = Configurational entropy (which is analogous to ΔS_{mix}),
R = Ideal gas constant,
x_i = Fraction of the sublattice i,
n = Number of components, and
c_j = Atomic fraction of component j.

As with all high-entropy materials, higher values of configurational entropy result in lower Gibbs free energy, which in turn points towards phase stability [10]. However, due to much higher degree of combinational complexity in HECs compared to HEAs, the construction of prediction models for phase stability of HECs is not as straightforward with just this approach. As of this writing, there are few works that have demonstrated the use of Gibbs free energy calculations for the prediction of HEC phase stability. Most published work on HECs simply relies on the intuitive approach of choosing a group of elements from the periodic table that lie close together. A few papers have, however, been published regarding the design of HEC materials by relying on descriptor-based approach for the construction of their prediction models [37].

For such models, the choice of descriptors is very important, as the use of descriptor assumes that there are common patterns in the desired materials which is accurately described by them. A very successful descriptor has been developed by Sarker et al. [10] called the Entropy Forming Ability (EFA), defined as

$$EFA = \left(\sqrt{\frac{\sum_{i=1}^{n} (H_i - H_{mix})^2}{\left(\sum_{i=1}^{n} g_i\right) - 1}} \right)^{-1} \tag{7}$$

Where

$n =$ Total number of sampled geometrical configurations,
$g_i =$ Degeneracy of i^{th} configuration,
$H_i =$ Enthalpy of i^{th} configuration, and
$H_{mix} =$ Mixed-phase enthalpy, which is approximated by

$$H_{mix} = \frac{\sum_{i=1}^{n} g_i H_i}{\sum_{i=1}^{n} g_i} \tag{8}$$

Large values of the EFA descriptor favor larger entropy values. Sarker et al. generated a total of 56 high-entropy carbides in their simulations and successfully synthesized 9 of them as well out of which 6 were single-phase HECs [38].

Liu et al. [39] formulated another useful descriptor δ, called the solubility parameter. For a binary solid solution, δ is defined as

$$\delta = \frac{\overline{R^*} (\Delta R^*)^2}{Z} \, \bar{G} \tag{9}$$

Where

$\overline{R^*} =$ Average effective lattice constant,
$\Delta R^* =$ Difference in effective lattice constant,
$\bar{G} =$ Average shear modulus, and
$Z =$ Number of formula units per unit cell.

When the number of components is greater than two, the average atomic solubility $\bar{\delta}$ can be determined by averaging the δ for all the separate binary solutions [39]. A low value of $\bar{\delta}$ indicates a high atomic solubility and hence, low internal strain energy. Liu et al. conclude this descriptor to be a high throughput screening method for high-entropy candidates.

Besides these, many other parameters such as the oxidization state and atomic size difference of the elements [40] have been observed to play a significant role in stabilization of single-phase high-entropy materials and can be very useful in the construction of a prediction model for phase-stability of HECs. A promising trend in the construction of these models is to use the results of empirical and Gibbs free energy calculations for combined models. Furthermore, computational modelling employing a range of methodologies including Density Function Theory (DFT), Calculation of Phase Diagrams (CALPHAD), Monte Carlo (MC) simulations, and Molecular Dynamic (MD) simulations to construct surrogate models using Machine Learning (ML) techniques [3]. Figure 2-5 illustrates a pipeline of material design for high-entropy materials.

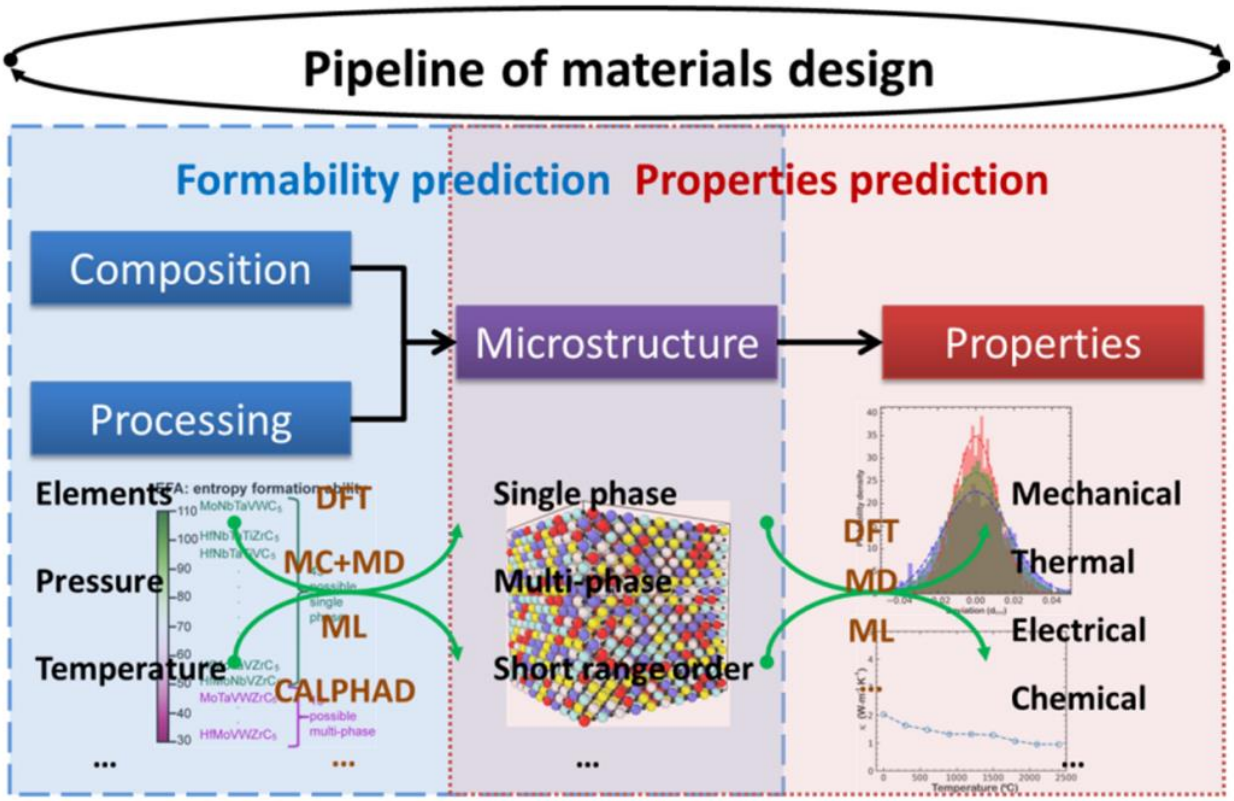

Figure 2-5 A pipeline of material design [3].

2.2.1. Important High-Entropy Ceramic systems

Although the development of HECs is still in its infant stages compared to HEAs, there are some very interesting systems that have been successfully synthesized and have demonstrated extraordinary properties. Some of these systems are highlighted below.

2.2.1.1. Spinel $(Co, Cr, Fe, Mn, Ni)_3O_4$

First synthesized by Dąbrowa et al. in 2018, the spinel [Fd-3m] $(Co, Cr, Fe, Mn, Ni)_3O_4$ high entropy oxide is the first HEC with a spinel structure. It was synthesized through solid state synthesis technique where equimolar oxide precursors were formed into 9 × 1.5 mm pellets under 200 MPa pressure. The precursor pellets were then free-sintered for 20 hours at $1050°C$ before being air quenched. Cooled sheets of aluminum were used to accelerate the process [41].

Grzesik et al. studied the defect structure and the chemical diffusion in the spinel $(Co, Cr, Fe, Mn, Ni)_3O_4$ high-entropy oxide and also characterized excellent thermal stability up to $1000°C$. Successful synthesis of single-phase spinel $(Co, Cr, Fe, Mn, Ni)_3O_4$ was achieved through solid state synthesis. Furthermore, partial oxygen pressure was also observed to have interesting effects on the defect structure and the chemical diffusion [8].

In this work, the precursors obtained from solvent deficient method resulted spinel oxides, although not phase-pure. However, a colleague (Jan Bernauer) worked on the synthesis of this oxide via solvent deficient method and was able to obtain this composition via calcination of the solvent deficient precursors in air.

2.2.1.2. Rock salt $(MgCoCuNiZn)O$

One of the earliest and most well-known HECs is the rock salt $(MgCoCuNiZn)O$ high-entropy oxide. This HEC system has been synthesized by Nebulized Spray Pyrolysis (NSP), a technique that is known to yield high-entropy oxides with very good crystallinity, using nitrate hydrates of transition metals as precursors and an aqueous solvent [42]. The development of this HEC system ignited great interest in the topic, especially for high-entropy oxides, followed by the successful synthesis of many derivative systems as well as completely different high-entropy oxides and other HEC classes [43].

Among other interesting characteristics, the rock salt $(MgCoCuNiZn)O$ high-entropy oxide and its derivates have demonstrated lithium superionic conductivity at room temperature, indicating great potential for reversible energy storage [2, 44].

2.2.1.3. Rock salt $(HfZrTaNbTi)Nx$

Contrary to other classes of HECs such as the high-entropy borides and high-entropy carbides, the bulk synthesis of high-entropy nitrides has been a difficult task and they've mostly been synthesized as only thin-films. Moskovskikh et al., however, successfully managed the bulk synthesis of the rock salt $(Hf_{0.2}Nb_{0.2}Ta_{0.2}Ti_{0.2}Zr_{0.2})N$ in 2020. Furthermore, they reported a three-step process for the bulk fabrication, which shows great promise for synthesizing bulk high-entropy nitrides. The steps of the process are: (i) high-energy ball milling (HEBM) of metal powders to produce reactive nanostructured mixture; (ii) combustion synthesis (CS) in a nitrogen atmosphere; and finally, (iii) spark plasma sintering (SPS) of the combustion products in a nitrogen environment for consolidation of the bulk high-entropy nitride systems [4].

Dippo et al. also reported bulk synthesis of high-entropy nitrides and carbonitrides, independent from Moskovskikh et al., including the synthesis of rock salt $(HfZrTaNbTi)N_x$ system. In their method, the powders of individual binary nitride precursors are first hand-mixed to achieve an equiatomic mixture, followed by conventional ball milling of the mixture and finally, SPS under vacuum [45].

Moskovskikh et al. reported hardness (up to $33\ GPa$) and fracture toughness (up to $5.2\ MPa.m^{1/2}$) demonstrated by the rock salt $(Hf_{0.2}Nb_{0.2}Ta_{0.2}Ti_{0.2}Zr_{0.2})N$ system, which is remarkably higher than estimations and the values reported for other binary or ternary nitrides, as well as all other HECs so far. This is a very interesting combination of properties which makes high-entropy nitrides very promising candidates for diverse practical applications that require special mechanical properties and is presumed to be a result of entropy stabilization and valence electron concentration optimization of the high-entropy nitride phase.

2.3. Synthesis of High-Entropy Ceramics

With the tremendous advantages that HECs have to offer comes the challenges related to their synthesis and processing. To ensure homogenous distribution of constituents within the high-entropy structure, several methods have been investigated and successfully applied. One of such methods that is frequently applied to obtain HECs is the solid-state reaction [37]. Other than that, wet chemical methods, solidification, field-assisted method, and epitaxial growth have also been investigated [3].

2.3.1. Solid State Reaction

In general, in the solid-state reaction approach, initially the precursor powders are ground and mixed, followed by subsequent heating at intermediate range of temperatures, typically $350°C - 450°C$ [46]. Afterwards, the powders can be ground or milled again in order to attain improved homogeneity. Lastly, the high-temperature sintering of these pre-milled/ground powders is done to obtain consolidated HECs [37]. The solid-state reaction occurs due to diffusion facilitated by pressure and elevated temperature. This method has been found to be suitable for synthesis of diverse HEC systems, such as, oxides, silicates, borides, carbides, nitrides, silicide, carbides etc. [37]. Synthesis of bulk high-entropy carbo-nitrides have also been reported via this route. One interesting example of novel solid-state synthesis approach is the formation of single-phase carbide high entropy ceramic $(Hf_{0.2}\ Ta_{0.2}\ Ti_{0.2}\ Nb_{0.2}\ Mo_{0.2}/Zr_{0.2}\ )C$ via self-propagating high-temperature synthesis (SHS), via mechanical activation (MA) of powder mixtures and mechanical synthesized (MS) materials. It was also reported that using this approach, achievement of higher densities and improved fracture toughness is possible by utilizing higher sintering temperatures [47].

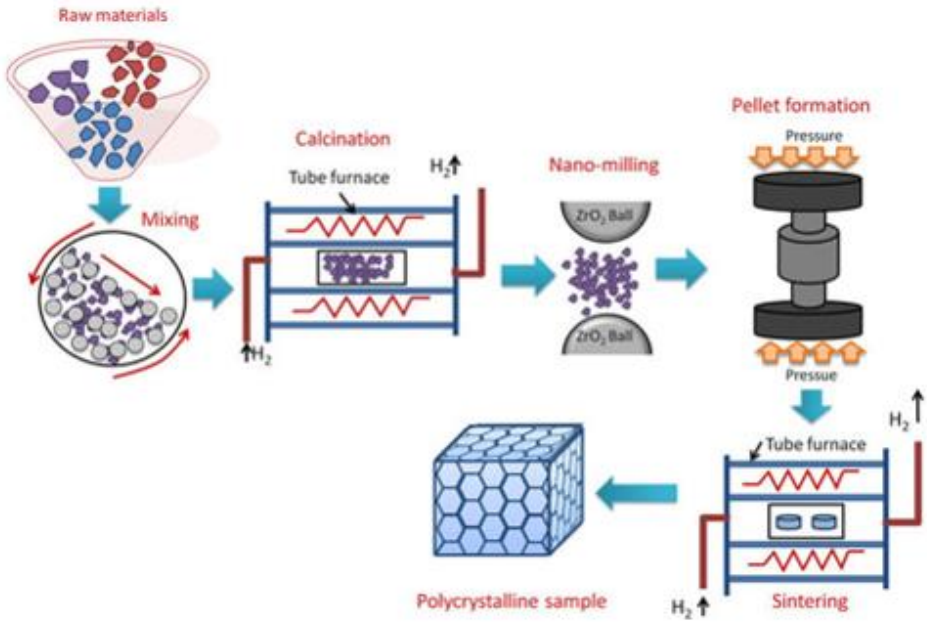

Figure 2-6 Schematic of processing ceramics by the solid-state reaction method [48].

2.3.2. Wet Chemical Methods

Wet chemical methods include the various synthesis routes where a liquid phase is always involved. These methods have been reported to be suitable for synthesis of different classes of high-entropy oxide ceramics. Some of the notable methods are namely co-precipitation, sol-gel synthesis, hydrothermal and

solvothermal methods, nebulized spray pyrolysis and flame spray pyrolysis. These methods enable better crystallinity and narrow particle size distribution to be accessible [37]. Hydrothermal method is also used in this work, to investigate formation of high-entropy nitrides and is discussed in detail in the next section. Nebulized spray pyrolysis utilizes principle of aerosol technology. The elevated temperatures assist the formation of product phases from the precursor solution. This method is also mostly known for synthesis of oxides. For instance, the formation of high entropy oxide systems based on rare-earths and transition metals have been reported [49-51].

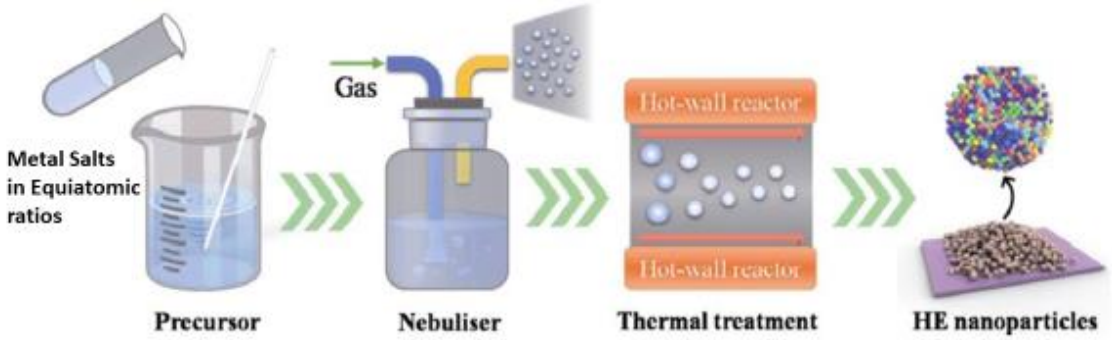

Figure 2-7 Schematic of Nebulized Spray Pyrolysis for synthesis of HECs [3].

2.3.3. Pulsed Laser Deposition

The synthesis of HECs via epitaxial growth has been known to utilize Pulsed Laser Deposition (PLD) technology for synthesis of high-entropy oxide systems. This method is quite useful for the growth of single crystals. More advantages include achievement of accurate compositional ratios, and avoidance of grain boundary segregation [37]. Contrary to other methods mentioned previously, this technique is capable of producing unique hetero-structures and super-lattices [52].

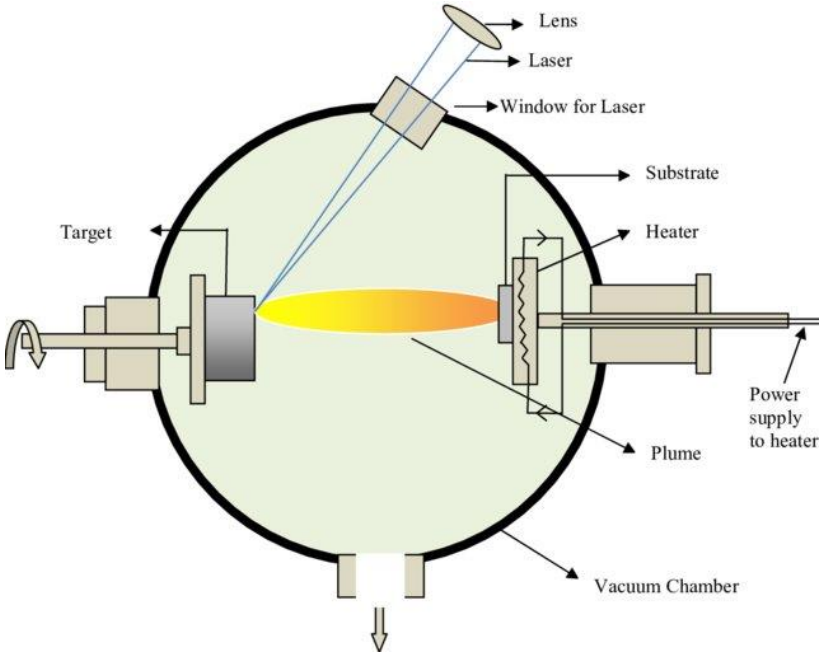

Figure 2-8 Schematic of Pulsed Laser Deposition (PLD) [53].

2.4. Solvent-Deficient Method

This technique has been fairly recent, first used by Smith et al [54]. In this method, hydrated metal nitrates or chlorides are ground together with ammonium hydrogen carbonate for up to 30 minutes. The reaction is initialized by applying pressure through the pestle and solid reactants turn into a slurry, following bubbling being observed in the slurry. When the bubbling has completely stopped, it indicates that the reaction is complete. The precursor obtained is then subjected to a heat treatment.

$$MSalt_y \cdot xH_2O + yNH_4HCO_{3(s)} \xrightarrow{Grind} Precursor(s) \xrightarrow{Rinse} Rinsed\ Precursor(s) \xrightarrow{Heat} nano\ M_aO_{b(s)}$$

This technique shares some resemblance with co-precipitation, but it doesn't involve addition of solvents, hence the term "solvent deficient". As a result, some useful features such as better crystallinity, and mesoporous morphology due to formation of agglomerates is in store. [55]

Smith et. al used this method to synthesize a variety of binary oxide nanoparticles. Since then, the technique has also proven to be quite useful for the synthesis of more systems like hydroxides and compositionally complex oxides such as perovskite $BiFeO_3$ and $Ba_{0.5}Sr_{0.5}Co_{0.8}Fe_{0.2}O_3$ and spinel structure $NiFe_2O_4$ [56-59]

This work also aims to explore whether this technique is suitable also for the synthesis of metal nitrides, by subjecting the precursors to heat treatment under ammonia flow.

Below, each step of this process is listed and explained further.

Step 1: Grinding of Metal Salts with Ammonium Hydrogen Carbonate

At this stage, hydrated metal salts (in this work, salt = NO_3^-) are ground with ammonium carbonate to obtain the precursor. The molar ratios are of significance here. The moles of bicarbonate are equivalent to the oxidation number of metal cation. This step is shown in Figure 2-9 , for the preparation of precursor for the multicomponent nitride investigated in this work. At the beginning, the reagents are put together Figure 2-9 , after the grinding process starts, the components become a slurry and bubbling starts, indicating reaction initiation Figure 2-9 . The process of grinding continues until the bubbling is not observed anymore Figure 2-9 Afterwards, the product is dried in an oven ($60°C$) for 2 hours and is further ground to obtain the precursor as fine powder Figure 2-9 .

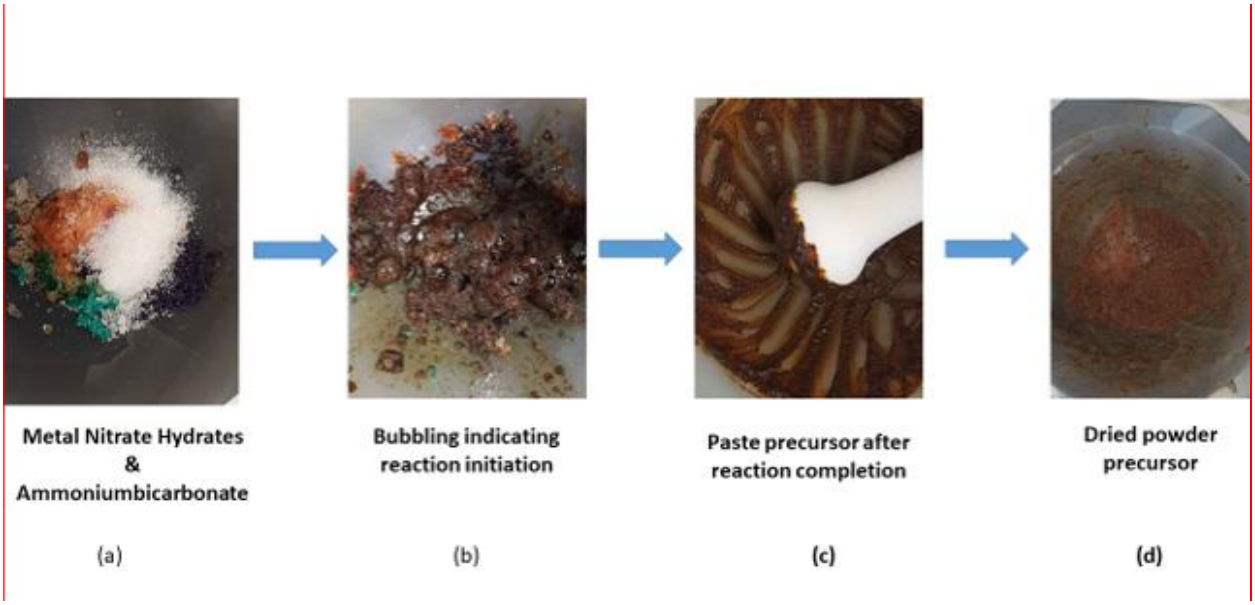

Figure 2-9 Synthesis of 5-component precursor via solvent-deficient method.

The hydration level of the metal salts used is of high significance here. Smith et. al found the minimum required hydrated salts to be hexahydrates, so that the enough water is released during the grinding to make the dissolution of the components possible. Higher hydration level gives shorter reaction times. If the hydrates do not have enough moles of water, a few drops of water can be added externally. As the reaction proceeds, the dissolved ions, depending on the metal salts, would result into products such as metal hydroxides, metal oxide hydroxides, hydroxide metal nitrates or carbonates, and metal carbonates. etc.

Possible reactions that could occur (smith et.al) [54]

$$M_y^+ + yOH^- \rightarrow M(OH)_{y(s)}$$

$$M^{3+} + 2OH^- + H_2O \rightarrow MOOH_{(s)} + H_3O^+$$

$$M^{2+} + OH^- + NO_3^- \rightarrow M(OH)(NO_3)_{(s)}$$

$$M^{3+} + OH^- + HCO_3^- + H_2O \rightarrow M(OH)(CO_3)_{(s)} + H_3O^+$$

$$M^{2+} + CO_3^{2-} + H_2O \rightarrow M(CO_3)_{(s)}$$

$$M^{4+} + 4OH^- + 4H_2O \rightarrow MO_{2(s)} + 4H_3O^+$$

After the reaction is complete and excess water dries up, ammonium salts are formed. This agglomeration can lead to useful properties such as mesoporous morphology after heat treatment.

$$NH_{4\,(aq.)}^{+} + NO_{3\,(aq.)}^{-} \rightarrow NH_4NO_{3\,(s)}$$

$$NH_{4\,(aq.)}^{+} + Cl_{(aq.)}^{-} \rightarrow NH_4Cl_{(s)}$$

Step 2: Rinsing

This rinsing step is usually only important when the metal salts used are chlorides. In this case, even after the thermal treatment, chloride impurities may remain in the product. These impurities occur, if NH_4Cl is present in the precursor. It decomposes at around $350°C$, dissociating in ammonia and HCl which can react with metal ions.

$$NH_4Cl \rightarrow NH_3 + HCl$$

Whereas, if nitrates are used, NH_4NO_3 is formed during grinding, which decomposes at about $170°C$, resulting in N_2O and moisture.

$$NH_4NO_3 \rightarrow 2H_2O + N_2O$$

At even higher temperature, it may also convert to ammonia and nitric acid [37].

The rinsing step could also be useful to obtain smaller crystallite size. Decomposition of NH_4NO_3 is exothermic, and results in a significant release of energy ($> 0.4\ \mu V\ mg^{-1}$), which causes grain growth [54]. Hence, removal of NH_4NO_3 before thermal treatment may prevent that.
In case the targeted material is oxides, rinsing may also prevent unwanted oxidation or reduction reactions during heat treatment in air.

In this work, the rinsing step was not carried out, since the salts used were hydrated metal nitrates, and the crystallite size was not a primary focus. Also, the heat treatment is carried out in ammonia, and not in air as the targeted compounds are nitrides.

The excess or unreacted ammonium hydrogen carbonate in the precursor is also not a problem. It dissociates into water, carbon dioxide, and ammonia at about $60°C$ [60]

$$NH_4HCO_3 \rightarrow CO_2 + H_2O + NH_3$$

Step 3: Thermal treatment

The thermal treatment is quite important, and is needed to synthesize the targeted metal oxides, and in this case, nitrides. The by products are degraded, and the reaction is carried out in air to obtain oxides. In this work, however, the focus has been to obtain nitrides, by thermal treatment under ammonia atmosphere. If the starting material has hydroxides, it would lose water, and if it has carbonates or nitrates, the thermal degradation would lead to the removal of CO_2 or NO_x gases, respectively. In this work, the thermal treatment is carried out in ammonia flow, so investigate whether this approach is suitable to obtain multiple component nitrides.

2.5. Urea and Glycine assisted Hydrothermal Method

Synthesis of compounds via wet chemical methods is known to be a very suitable approach for achieving homogenous compounds. Hydrothermal method is one of such techniques and is a well-known method for obtaining fine powder particles. Compared to solid-state methods, this approach is much more efficient and convenient for synthesis of powder particles, and it is quite economical and scalable process. Through this approach, the resultant product is obtained through formation of precipitates of the hydrolyzed ions in saturated solution. Furthermore, another important advantage to this process is improved crystallinity [61].

A lot of parameters, such as solvent type, temperature, reaction time, PH etc. influence the precipitate growth of the product. Depending on what parameters need to be controlled and what conditions need to be maintained in the hydrothermal reaction, the reagents are chosen. For instance, a reducing agent is added if the goal is to avoid oxidation of ions[61].

In this work, metal nitrate hydrate salts have been dissolved in deionized water, and urea and glycine have been added to assist the hydrothermal synthesis.

The hydrothermal method involves placing the hydrothermal fluids in Teflon lined containers, which are enclosed in high-pressure steel vessels. These autoclaves are then subjected to high temperature, and the solvent inside generates pressure, and reaction proceeds under high pressure and temperature conditions. Under hydrothermal conditions, urea decomposes around $120°C$, resulting in ammonium hydroxide and carbon-dioxide gas [62]. The reaction that occurs is stated below.

$$(NH_2)_2CO_{(aq)} + 3H_2O_{(l)} \rightarrow 2NH_4OH_{(aq)} + CO_{2\,(g)}$$

The partial pressure inside the vessel elevates rapidly and the gas is dissolved in the reaction medium. Urea may also provide carbonate (CO_3^{-2}) ions, which can promote a reducing environment in the reactor as well [61]. For the five-component precursor synthesized via hydrothermal approach in this work, this was likely the case, as the XRD results showed indication of formation of metal carbides.

The hydrolysis of urea, along with release of carbon-dioxide gas, which is responsible for escalated pressure, promotes reaction between precursors, resulting in anisotropic crystal growth and oxide crystallization as well, requiring minimal temperature and reaction times [63].

Even though Urea may also be a source of ammonia, it is not very common, and may take relatively long reaction times. Although it has been reported to be useful regarding synthesis of iron(III) phosphates and also in the formation of other interesting compounds such as $Fe(NH_3)_2PO_4$ [64].

In this work, although the use of urea was based on the goal of achieving some nitrogen incorporation into the precursors, however, the XRD results did not indicate any nitrogen incorporation into the precursors.

Glycine assisted hydrothermal approach is also a well-investigated route [65, 66].

Metal salts can be hydrolyzed in aqueous solution to obtain hydroxides, along with release of protons. It is likely that the protons interact with NH_2 group of glycine to give NH_3^+ with counter NO_3^- or Cl^- ions, based on whether the metal salts used were nitrates or chlorides.

This approach has been reported to be suitable for synthesis and controlled growth of Fe_2O_3 nanoparticles [67].

In this work, the precursor prepared for binary reference material system Fe_2N resulted in Fe_2O_3 particles as well, and the initial metal salt used was iron nitrate nona-hydrate. Based on the literature, the following reactions can be predicted to have occurred [67].

$$Fe(NO_3)_3 + NH_2CHCOOH \xrightarrow{yields} Fe(OH)_3 + NH_4NO_3 + CHCOOH$$

$$Fe(OH)_3 \xrightarrow{yields} FeO(OH) \xrightarrow{yields} Fe_2O_3$$

Glycine, after incorporating the proton, links with $Fe(OH)_3$ through electrostatic interactions and hydrogen bonding, and hence, enables control over particle size [67].

The metal salt to glycine ratio employed in this work was 1:4, in order to obtain a greater surface-area to volume ratio of precursor particles, so that the exposure to ammonia is maximum during the subsequent thermal ammonolysis step.

3. Synthesis and Characterization Techniques

This section discusses the particulars of synthesis methods employed in this work, and the characterization methods used to analyze the resultant materials.

3.1. Synthesis

3.1.1. Chemicals

The reagents used were hydrates of Iron (III) Nitrate, Cobalt (II) Nitrate, Chromium (III) Nitrate, Manganese (II) Nitrate, and Nickel (II) Nitrate. Additionally, Urea, Glycine, and Ammonium Hydrogen Carbonate were also used. All these chemicals were purchased from *Sigma Aldrich*.

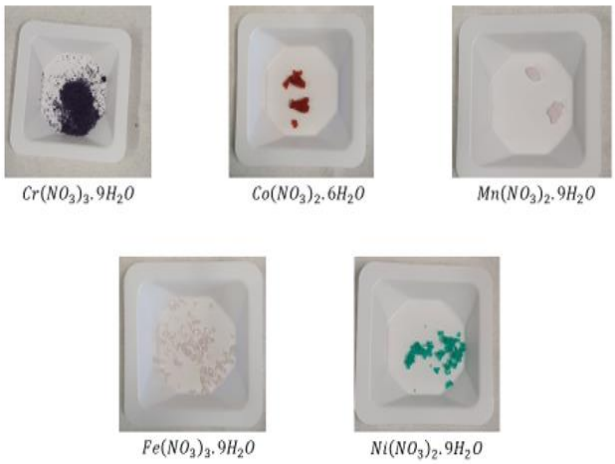

Figure 3-1 Hydrates of transition metal nitrates used

3.1.2. Solvent-Deficient Method

The precursors for two material systems were synthesized via this method by following the instructions from Section 2.4. Table 3-1 and Table 3-2 give molar ratios and quantities of the reagents used for precursors 1 and 4, respectively. The hydrates of metal nitrates were ground together with ammonium bicarbonate for 20 minutes, and then air-dried in an oven at $60°C$ for 2 hours.

Reagents	Molar Ratios	Mass (g)
$Fe(NO_3)_3.9H_2O$	1	1.616
NH_4HCO_3	3	0.949

Table 3-1 Molar ratios of reagents in Precursor 1.

Reagents	Molar ratio (Metal Nitrate: Ammonium Bicarbonate)	Mass (g)
$Cr(NO_3)_3.9H_2O$	1:3	0.40015
$Co(NO_3)_2.6H_2O$	1:2	0.29103
$Mn(NO_3)_2.H_2O$	1:2	0.19695
$Fe(NO_3)_3.9H_2O$	1:3	0.40400
$Ni(NO_3)_2.6H_2O$	1:2	0.29083

Table 3-2 Molar ratios of reagents in Precursor 4.

3.1.3. Urea and Glycine Assisted Hydrothermal Method

The precursors for the two material systems studied were also prepared via hydrothermal synthesis. Table 3-3 and Table 3-4 gives molar ratios used for precursors 2 and 3, respectively. The metal nitrates were first dissolved in deionized water, and afterwards urea and glycine were added to the solution. This solution was stirred for 30 minutes. Afterwards, the Teflon liners of hydrothermal reactors were filled with the solution up to 1/3rd of the available volume inside the Teflon liners (6 ml). The autoclaves were closed and tightened thoroughly, and then exposed to $170°C$ for $24\ hrs$. The schematic diagram of a typical hydrothermal reactor is shown in Figure 3-2 .

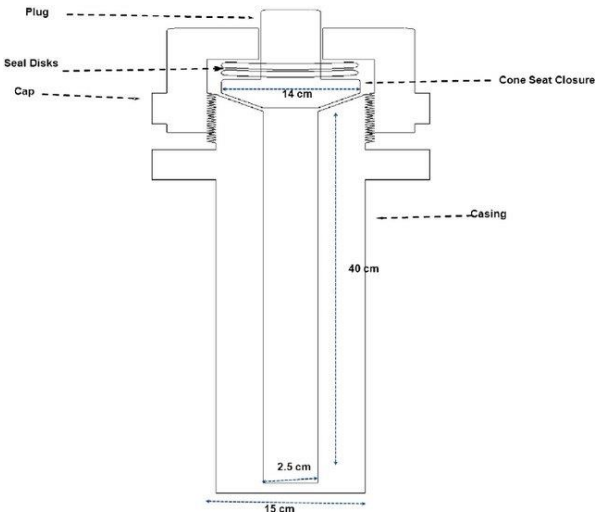

Figure 3-2 Schematic of a typical hydrothermal reactor.

Reagents	Molar Ratios	Mass (g)
$Fe(NO_3)_3.9H_2O$	1	1.616
$CO(NH_2)_2$	0.2	0.048
$C_2H_5NO_2$	4	1.201

Table 3-3 Molar ratios of reagents in Precursor 2.

Reagents	Molar ratio	Mass (g)
$Cr(NO_3)_3.9H_2O$	0.2	0.800
$Co(NO_3)_2.6H_2O$	0.2	0.582
$Mn(NO_3)_2.H_2O$	0.2	0.394
$Fe(NO_3)_3.9H_2O$	0.2	0.808
$Ni(NO_3)_2.6H_2O$	0.2	0.581
$CO(NH_2)_2$	0.2	0.120
$C_2H_5NO_2$	4	3.003

Table 3-4 Molar ratios of reagents in Precursor 3.

3.1.4. Thermal Ammonolysis

The ammonolysis of precursors was done at different target temperatures, however the Ammonia gas flow rate, and heating and cooling rates of the furnace were kept the same for all reactions. The ramp rate of $100°C$ was used for all experiments, and the gas flowrate was $50\ ml/min$. For each experiment, the tube was vacuumed 3 times, and purged with Argon between each cycle, before proceeding with the ammonolysis.

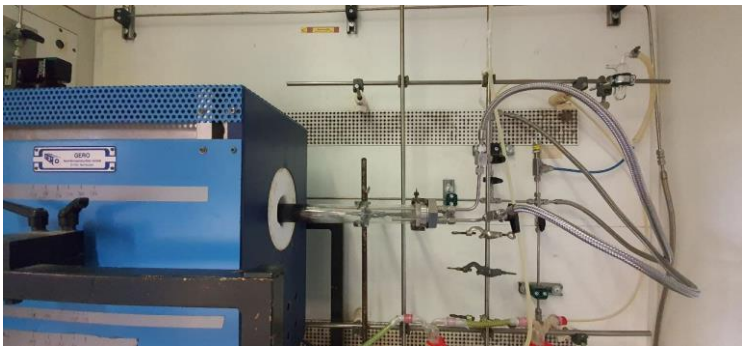

Figure 3-3 Typical setup for Ammonolysis; on the left is the furnace, and the sample is put inside a Schlenk tube, which is sealed and connected to gas inlet and outlet, for constant ammonia flow during the heating cycle.

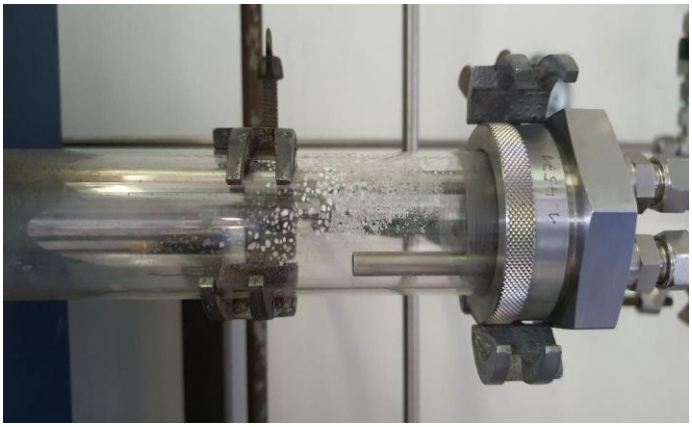

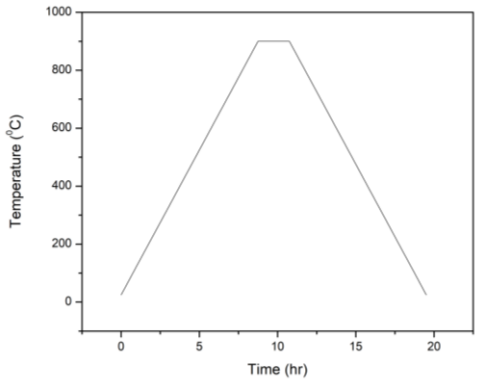

Figure 3-4 Left: A magnified view of the Schlenk tube shows signs of sublimation after ammonolysis of 5-component solvent-deficient precursor; Right: Thermal profile for Ammonolysis reaction at 900°C for 2 hours.

3.1.5. Thermal Annealing

Some of the products obtained after ammonolysis of precursors synthesized via solvent-deficient method were subjected to thermal annealing at $1250°C$ for 3 hours. Alumina furnace was used for this treatment, and the samples were placed in silicon carbide crucibles, which were then placed in the furnace and subjected to thermal annealing in Argon atmosphere. For this treatment as well, the furnace chamber was vacuumed and purged with argon three times alternately. Thermal profile of this treatment is shown in Figure 3-5 .

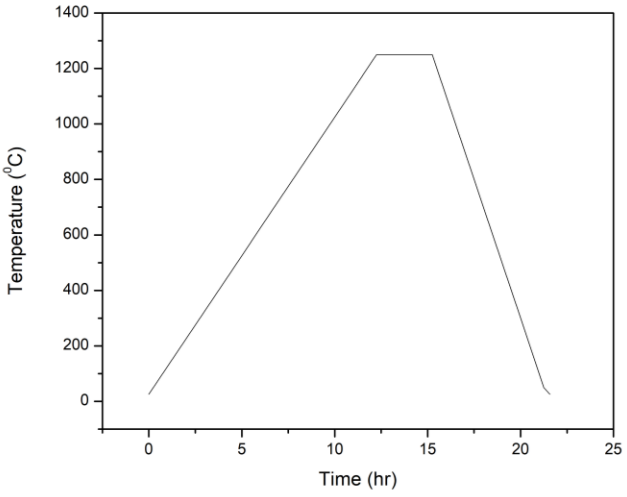

Figure 3-5 Thermal profile for high-temperature annealing.

3.2. Characterization Techniques

3.2.1. X-Ray Diffraction (XRD)

X-Ray Diffraction, or XRD, is a powerful nondestructive technique for characterizing crystalline materials. It provides information on structures, phases, preferred crystal orientations (texture), and other structural parameters, such as average grain size, crystallinity, strain, and crystal defects. X-ray diffraction peaks are produced by constructive interference of a monochromatic beam of X-rays scattered at specific angles from each set of lattice planes in a sample. Figure 3-6 shows set up that was used to take measurements for this project.

Figure 3-6 The XRD setup used in this this work.

XRD's mechanism is based on the principle of diffraction angle measurement when x-rays leave the sample that make certain pattern of peaks which are further evaluated by Bragg's law. William Lawrence Bragg introduced a law defining the space between atoms in a crystal to the angle at which x-rays are scattered by striking the crystal. Mathematical form of Bragg's law is:

$$n\lambda = 2d \sin\theta$$

Where;

λ = wavelength of x-ray beam
d = spacing between crystal planes
θ = angle of x-rays scattering

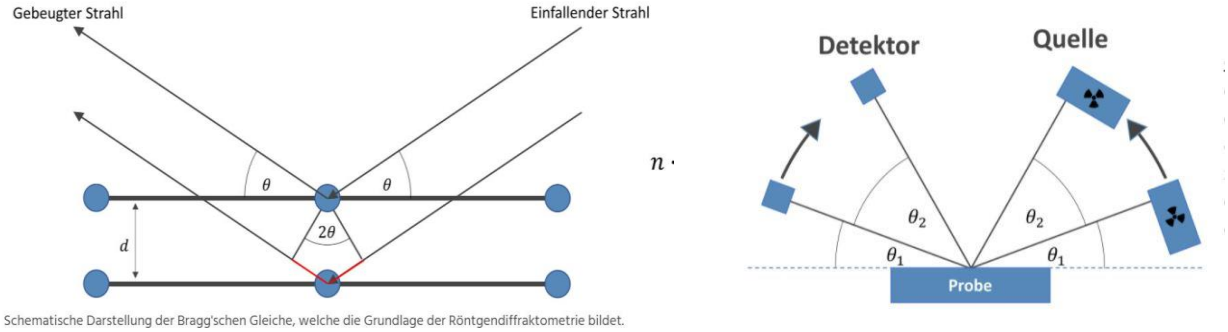

Figure 3-7 Left: Schematic for the X-Ray Diffraction principle; Right: Schematic showing the measurement mechanism (The diagram has been taken from the website of Materialwissenschaftliches Labor Dr. Paul Rossi).

3.2.1.1. Sample Preparation

Samples were prepared for measurement by placing a transparent foil on the sample holders. The powder was then placed on the foil, and a few drops of XRD glue were added to make the powder particles stick firmly to the foil. The samples with glue were then cured under a lightbulb for 10 minutes to evaporate the XRD glue and make the sample dry. Another foil is then placed over the powder, and the metal ring is then screwed over the holder.

Figure 3-8 Preparation of the samples under the lightbulb.

Figure 3-9 Some of the XRD samples from this work.

3.2.2. Raman spectroscopy

This technique is based on the Raman effect, according to which when incident light excites molecules, the molecules will reflect light in a different wavelength, that is, inelastic scattering of monochromatic laser light. An energy deviation due to the interaction of phonons and laser light gives information about the phonon modes of the material. The wavelength of the reflected light has information about the chemical components and allows the detection of compounds. This technique is based on the inelastic scattering process and detects vibrations related to change in polarizability [68]. For the spectroscopic measurements in this work, a green laser source i.e., a wavelength of 514 nm was used.

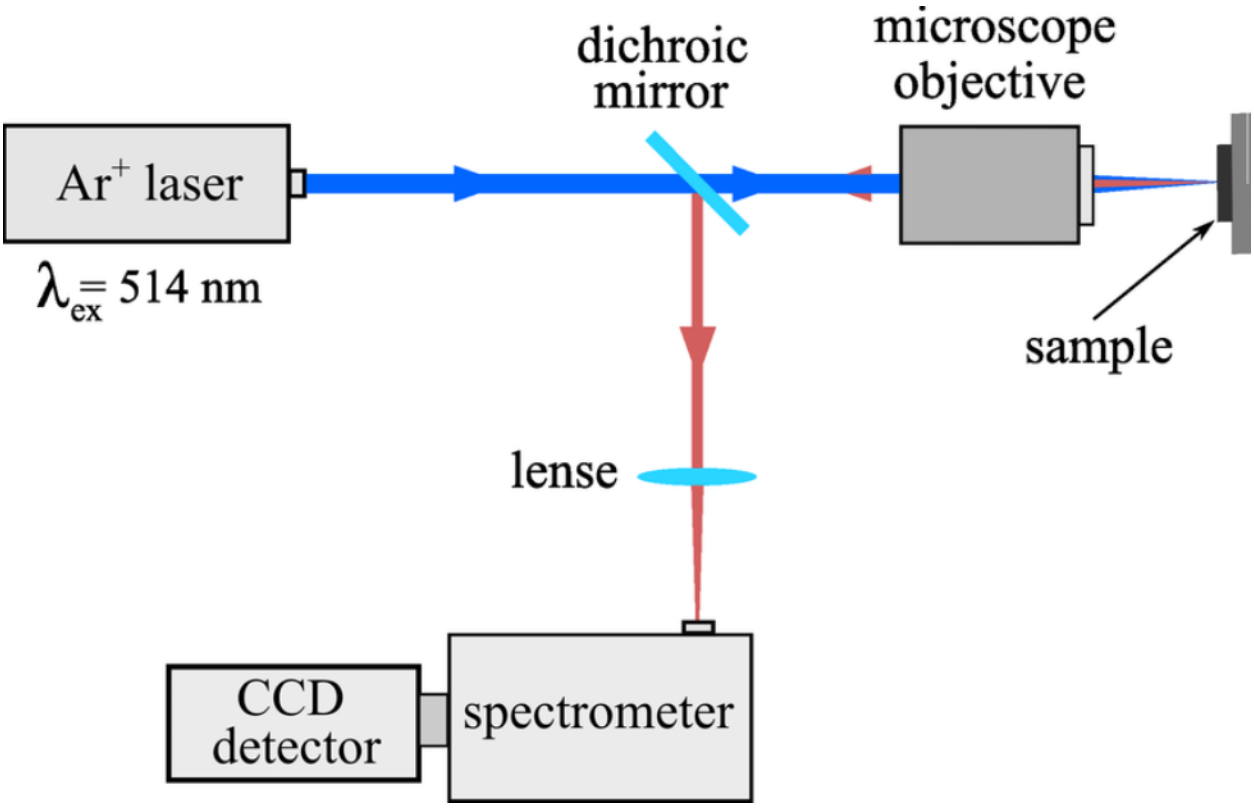

Figure 3-10 Working Principle of Raman Spectroscopy [69].

3.2.3. Thermo-gravimetric Analysis (TGA)

TGA is a very useful technique for analyzing thermal stability of materials. The technique is based on the working principle that the mass changes in the sample are recorded as it is heated to elevated temperatures. The set-up requires a sensitive mass balance to record mass changes and a programmable furnace to regulate the temperature of the specimen. It has a micro-furnace, the temperature of which can be brought down quickly. The heating element is usually platinum that allows temperatures up to $1000°C$. The modern set-up also includes a computer which computes the percent weight loss, and the heating rate can be varied from $0.1 - 200°C$/min [70]. It can also be coupled with infrared spectroscopy and mass spectrometry to obtain information about the decomposition products.

The TGA measurements done in this work were done using the heating rate $10°C/min$, under Ammonia atmosphere.

3.2.4. Differential Thermal Analysis (DTA)

The working principle of this technique is such that the temperature difference of sample and a reference is recorded, and the thermo-gram is generated, which is a plot of the temperature difference. It gives information about the possible exothermic or endothermic reactions that the specimen would undergo. The temperatures for changes such as phase transitions, melting or decomposition, crystallization etc. can be determined. The usual heating rates are $10°C$ or $20°C$/min. This technique is particularly more relevant in characterizing mixtures of polymers [70].

In this work, the DTA measurement is done using heating rate of $10°C$/min under ammonia atmosphere up to $1000°C$ for precursors synthesized via solvent-deficient approach.

4. Results and Discussion

4.1. Precursors

4.1.1. Precursor 1

The precursor prepared via solvent deficient method in the work of Smith et. al. results in $NH_4NO_3 + FeOOH \cdot 0.4H_2O$, if the precursor is only dried and not rinsed, as was the case for the experiments in this work [54].

The Raman spectrum of this precursor is shown in Figure 4-1. The peak positions at 1049 cm^{-1} and 1320 cm^{-1} correspond to Raman vibrational modes of NH_4NO_3 [71]. The signals between 150 cm^{-1} and 707 cm^{-1} are possibly due to $FeOOH$ and the broad peak around the region 3150 cm^{-1} indicates $O-H$ stretching [72].

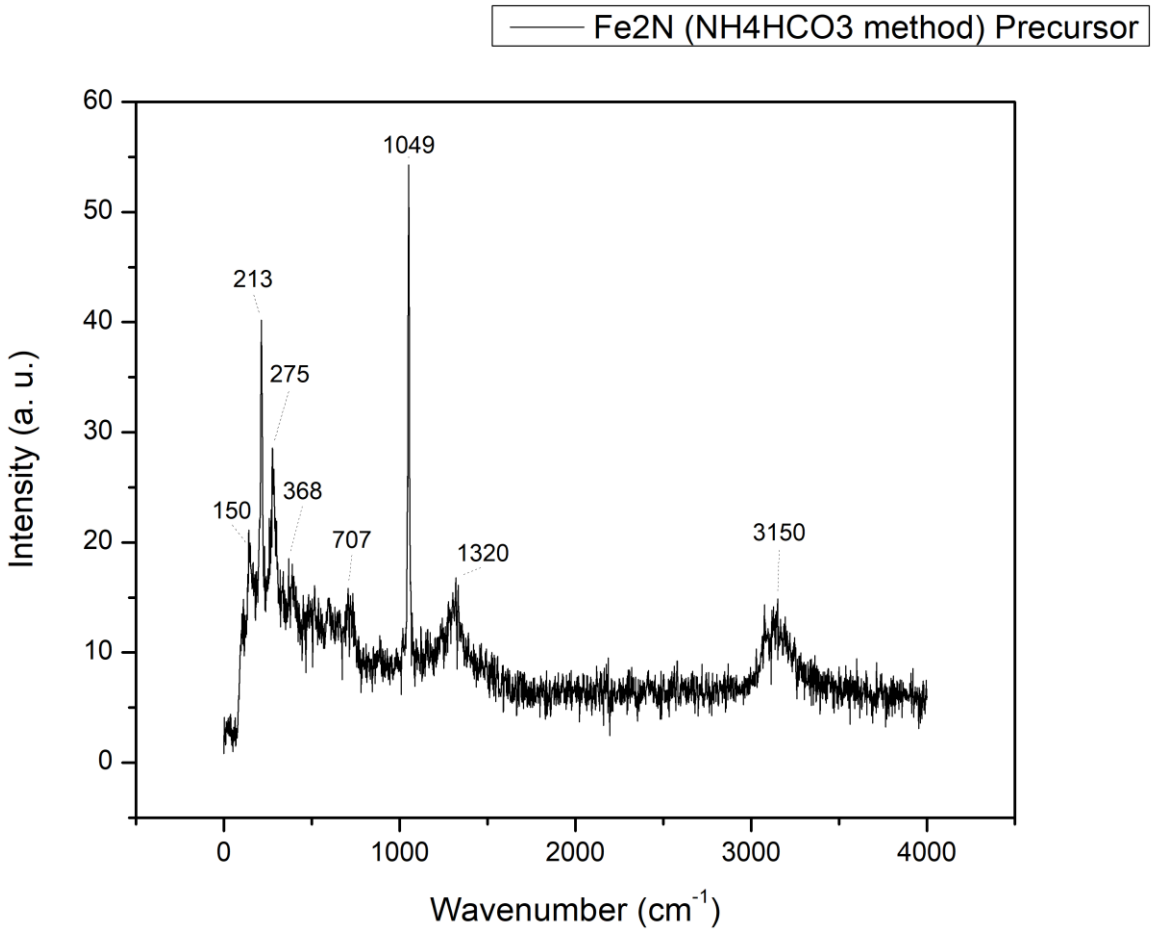

Figure 4-1 Raman Spectrum of Precursor 1.

Figure 4-2 shows TGA plot for precursor 1 heated at the rate $10°C$/minute up to $1000°C$ in Ammonia atmosphere. Below $200°C$, a total of negative mass change is -5.2% accompanied by two endothermal signals in DTA thermos-gram. This is possibly due to release of water of crystallization.

$$MX.H_2O \xrightarrow{yields} MX + H_2O$$

Afterwards, there is a major weight-loss indication at about $300°C$, i.e -60.3% and -9.8%. These mass changes give two exothermal signals in DTA plot.

Ammonium nitrate has been reported to decompose at about $210°C$ [73] so the weight-loss indication can be attributed to the decomposition of ammonium nitrate, and other nitrate containing materials.

$$NH_4NO_3 \xrightarrow{yields} N_2O + 2H_2O$$

Since ammonia atmosphere provides reducing as well as nitriding potential [74], hydroxides can convert to oxides, and following reactions have possibility to occur,

$$NH_3 + Fe_2O_3 \xrightarrow{yields} \frac{1}{2}\, Fe_4N + 3\, H_2O \; + \; \frac{3}{4} N_2$$

$$Fe_4N + 2NH_3 \xrightarrow{yields} Fe + N_2 + H_2$$

Elemental iron can convert to $Fe_3N_{1\pm x}$ or $\zeta - Fe_2N$ under decomposition of ammonia [75]. This is confirmed by the XRD results of ammonolyzed samples.

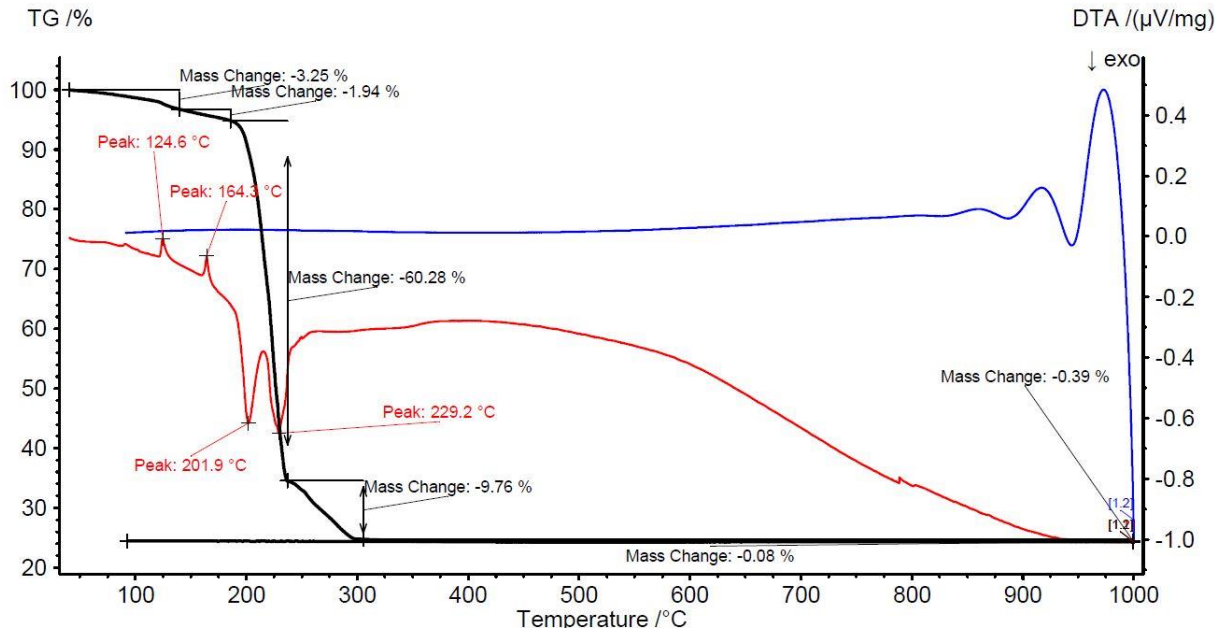

Figure 4-2 TGA and DTA plot of precursor 1.

4.1.2. Precursor 2

The XRD pattern in Figure 4-3 confirms the formation of phase pure hematite Fe_2O_3 as the precursor synthesized by hydrothermal method. The pattern was matched with that of Fe_2O_3, based on reference [76], and also using the database ICSD, MaterialsProject, COD, and the data matched exactly with the Fe_2O_3 ($R\bar{3}c$) entries.

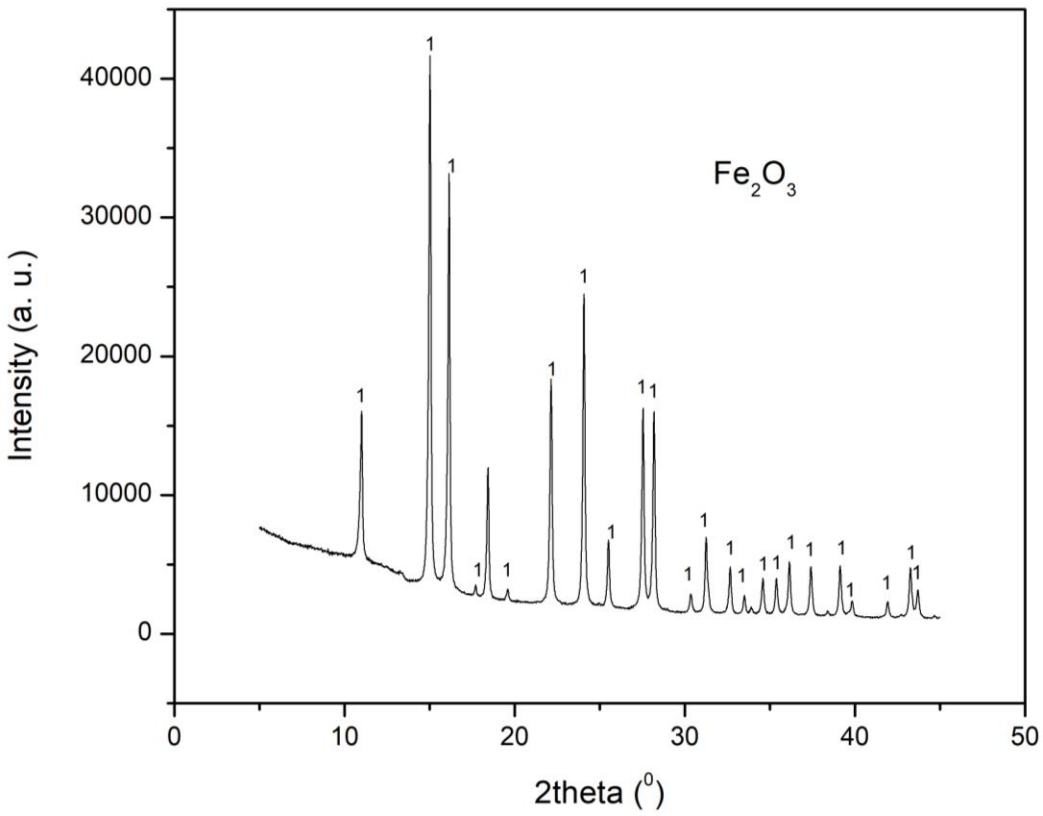

Figure 4-3 X-Ray Diffraction Pattern of Precursor 2.

The Figure 4-4 shows Raman spectrum of precursor 2. The Raman shifts at 205 cm^{-1}, 268 cm^{-1}, 484 cm^{-1}, 613 cm^{-1}, and 1279 cm^{-1} can be attributed to hematite. [77]

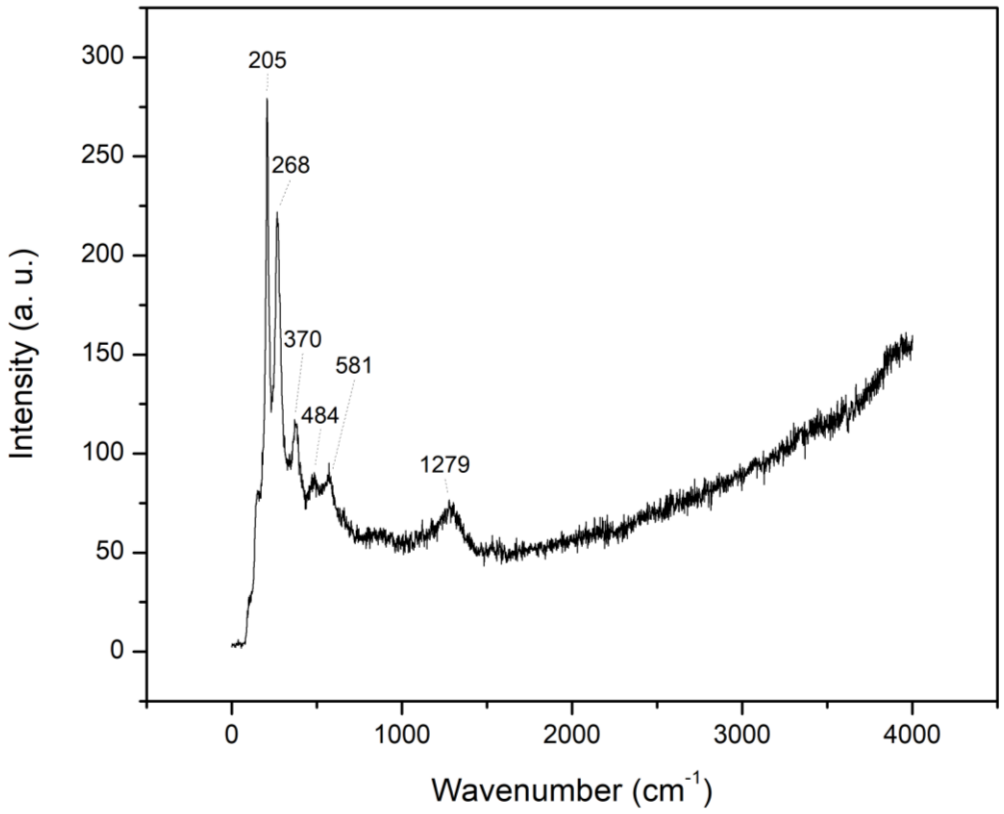

Figure 4-4 Raman spectrum of precursor 2.

4.1.3. Precursor 3

The XRD pattern (Figure 4-5) of this precursor indicates that the constituent elements have formed carbonate phase, a the pattern strongly matches carbonates of Iron and Manganese belonging to space group $R\bar{3}c$ [78] [79], and other transition metals present are likely also incorporated.

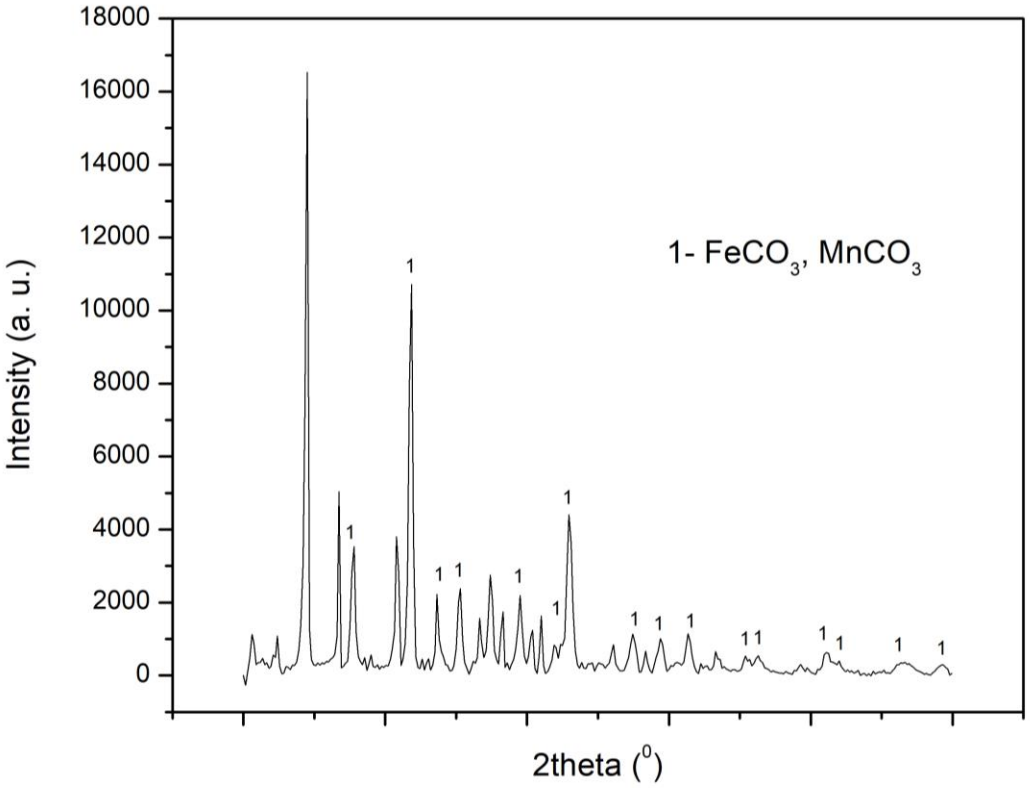

Figure 4-5 XRD pattern of precursor 3.

Figure 4-6 shows Raman spectrum of precursor 3, and the peak positions 191 cm^{-1}, 290 cm^{-1}, 500 cm^{-1}, and 870 cm^{-1} can be attributed to siderite $FeCO_3$, according to standard reference spectrum RRUFF ID: R040034. The broad peaks at 1360 cm^{-1} and 1530 cm^{-1} indicate D and G bands, characteristic to carbon-containing materials. The D band relates to the degree of structural defects in carbon, and G band is due to the Raman-active modes of sp^2 carbon atoms [80]. The region around 2800 cm^{-1} is the 2D or G' region due to carbon [81]. The positions at 191 cm^{-1}, 290 cm^{-1} and 663 cm^{-1}, are also characteristic to transitional lattice mode (T), liberational lattice mode (L), and v4 of $MnCO_3$ respectively [82].

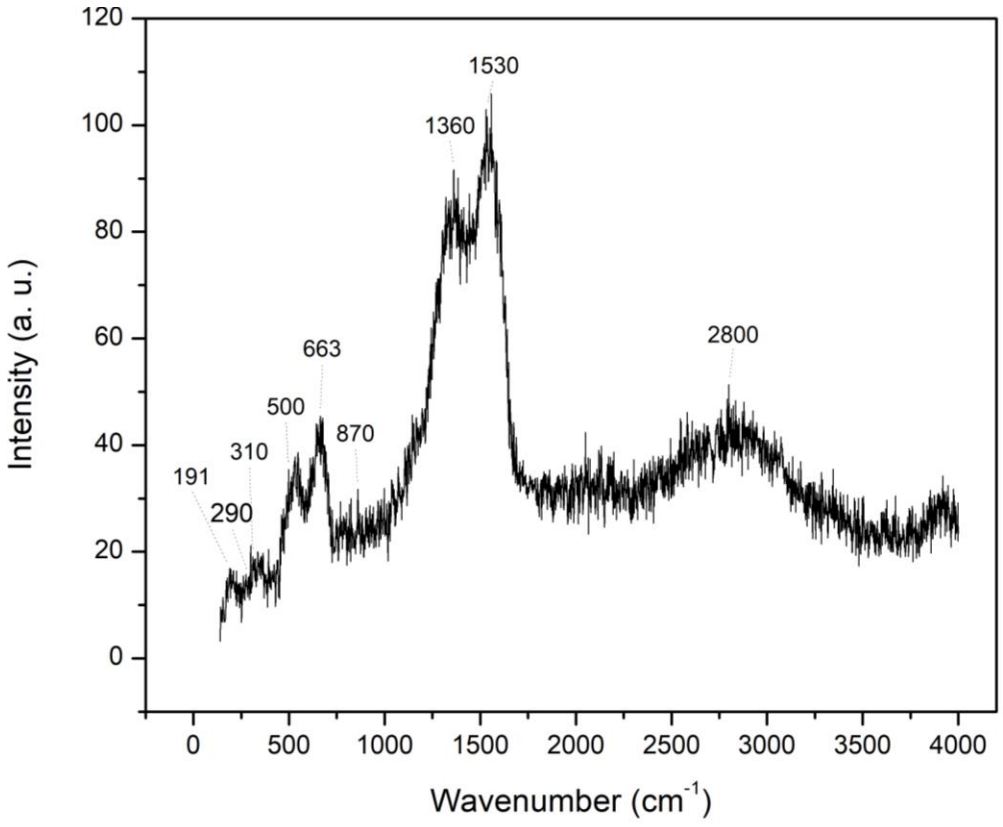

Figure 4-6 Raman spectrum of precursor 3.

4.1.4. Precursor 4

The composition of this precursor is not simple to determine, as five metal nitrates were used, however, an estimate can be done by comparison with precursors prepared by single metal salt. Considering the work of Smith et. al., the Table 4-1 gives the composition each metal nitrate would individually give.

Metal Nitrate	Resultant Precursor after Drying
Fe^{3+} (nitrate)	$NH_4NO_3 + FeOOH \cdot 0.4H_2O$
Co^{2+} (nitrate)	$NH_4NO_3 + Co(OH)_2 + Co_2(OH)_3(NO_3) + Co(OH)(NO_3) \cdot H_2O$
Ni^{2+} (nitrate)	$NH_4NO_3 + Ni(OH)_2 + Ni_3(OH)_4(NO_3)_2$

Table 4-1 Precursor composition.

The ions M^{2+}, M^{3+}, NO_3^-, NH^{4+} , HCO_3^-, OH^- are formed, and react to produce products such as carbonates, hydroxyl-carbonates, hydroxides etc. It can be assumed that similar products are formed via nitrates of chromium and manganese. Figure 4-7 shows Raman spectrum of the multicomponent precursor. It confirms the presence of NH_4NO_3 corresponding to positions 1049 cm^{-1}, 1304 cm^{-1} and 1662 cm^{-1} [71]. The shifts at 136 cm^{-1} and 707 cm^{-1} can be attributed to $CoOOH$ and $FeOOH$ [83]. The peaks 706 cm^{-1}, 1121 cm^{-1}, 1390 cm^{-1} correspond to Raman modes of $Mn(CO)_3$ [84]. The peak positions 1390 cm^{-1} and 3142 cm^{-1} is due to water of crystallization. [85] To sum up, the presence of hydroxides of transition metal oxides, and metal carbonates can be concluded.

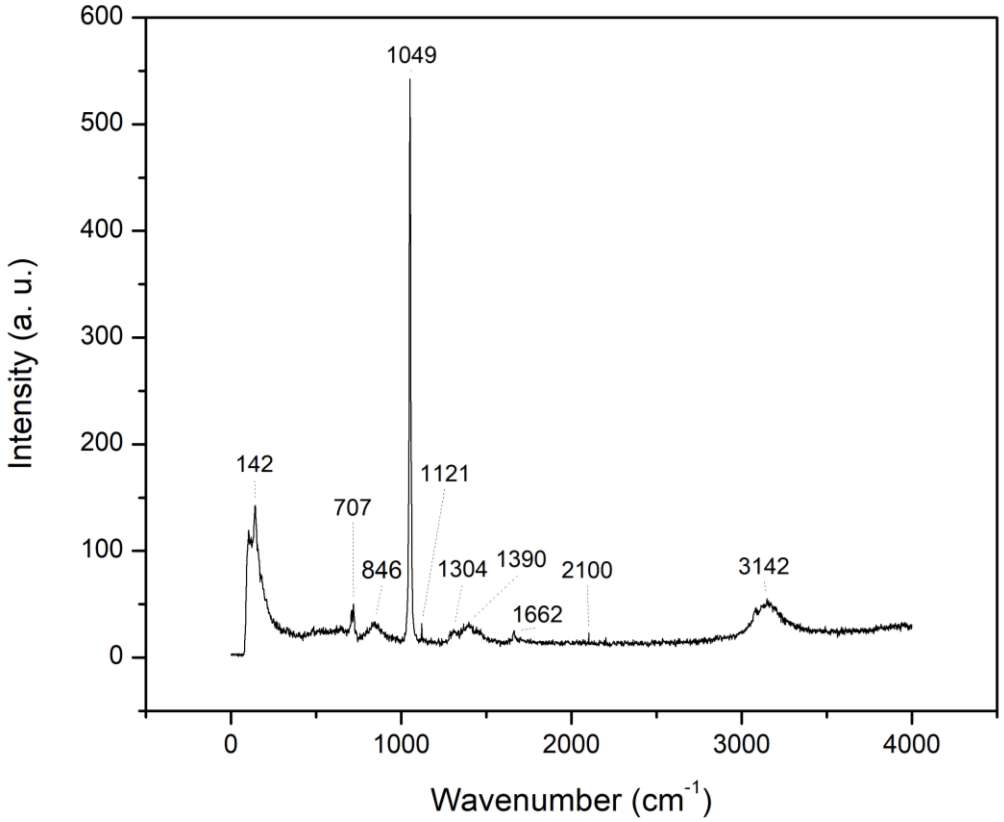

Figure 4-7 Raman spectrum of Precursor 4.

Figure 4-8 shows TGA plot for precursor 1 heated at the rate $10°C$/minute up to $1000°C$ in Ammonia atmosphere. A mass change of -3.13% is observed at $123.7°C$ and $147.4°C$, accompanied by endothermic signals in DTA, which is likely due to release of bound water. Afterwards, there is massive weight-loss of -61.76% at $218.7°C$, indicating exothermic signal in DTA thermos-gram. At about $500°C$, there is another mass change -8.01%, which is also an exothermic reaction. After this, the mass remains approximately unchanged.

The TGA plot is quite similar to the one for precursor 1, and similar reactions can be attributed to the weight-loss profile. However, the XRD results show tendencies of oxide formation, and alloy formation over nitrides. Compared to the TGA plot of precursor 1, there is an additional signal of weight-loss of -8.1% at around $500°C$. The work of Smith et al. indicates that salts of manganese can give carbonate precursor via solvent deficient method. Hence, this weight-loss signal can possibly be due to thermal decomposition of $MnCO_3$ [86].

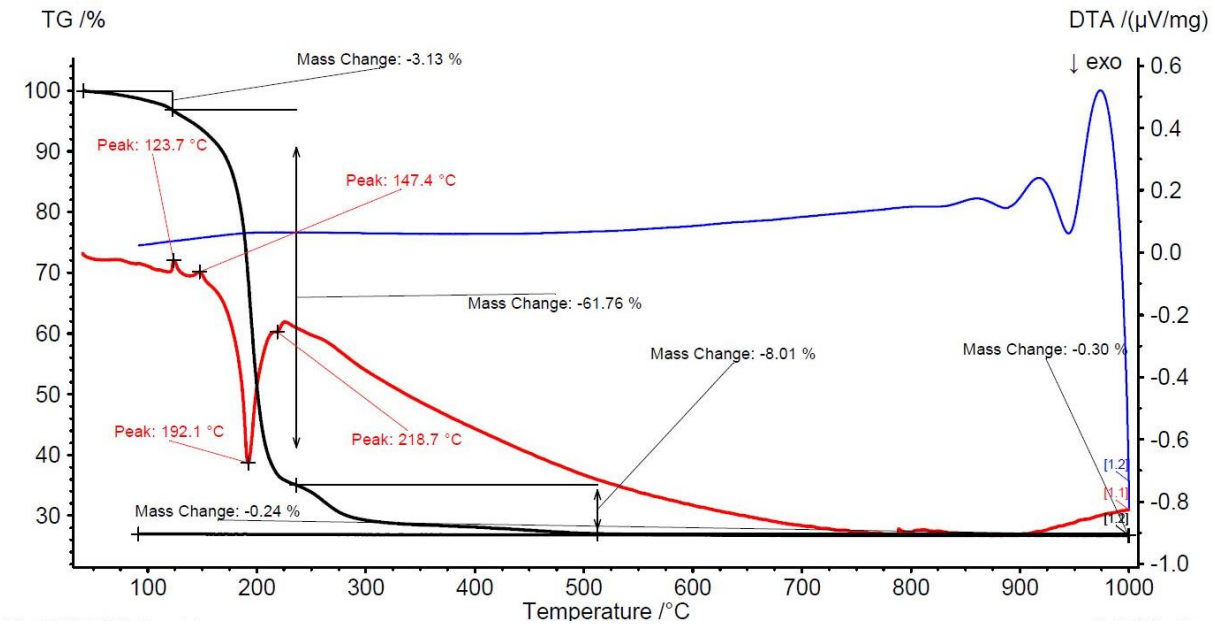

Figure 4-8 TGA and DTA thermogram of precursor 4.

4.2. Experiments

Starting Material	Ammonolysis Temp (°C), Time (h)	Thermal Annealing in Argon Temp (°C), Time (h)
Precursor 1	$900°C$, 2h	
Precursor 2	$900°C$, 2h	
	$600°C$, 2h	
Precursor 3	$900°C$, 2h	
	$500°C$, 2h	
Precursor 4	$900°C$, 2h	$1250°C$, 3h
	$500°C$, 2h	$1250°C$, 3h
	$500°C$, 5h	
	$200°C$, 5h	

Table 4-2 Summary of the experiments performed in this work.

4.2.1. Experiment 1 a: Precursor 1 Ammonolyzed at $900°C$ for 2h

The XRD pattern for this system is presented in Figure 4-9. The strong reflections indicate presence of Fe_2N [87, 88]. The possibility of incorporation of Fe_3N cannot be ruled out, as the patterns for Fe_2N and Fe_3N are very similar, while Fe_2N has an extra reflection at 2θ value of $45°C$. The shoulder at the peak indicates possibility of phases with two different nitrogen concentrations. This could be due to formation of N-rich areas at the surface, and N-deficient areas in the core of the powder particles. Longer reaction times may be necessary to incorporate more nitrogen to the cores. The reflections with relatively small reflections are likely an indication of Fe_4N, as compared with the standard pattern in ICSD[89]. However, the concentration of this phase is very small, as compared to Fe_2N.

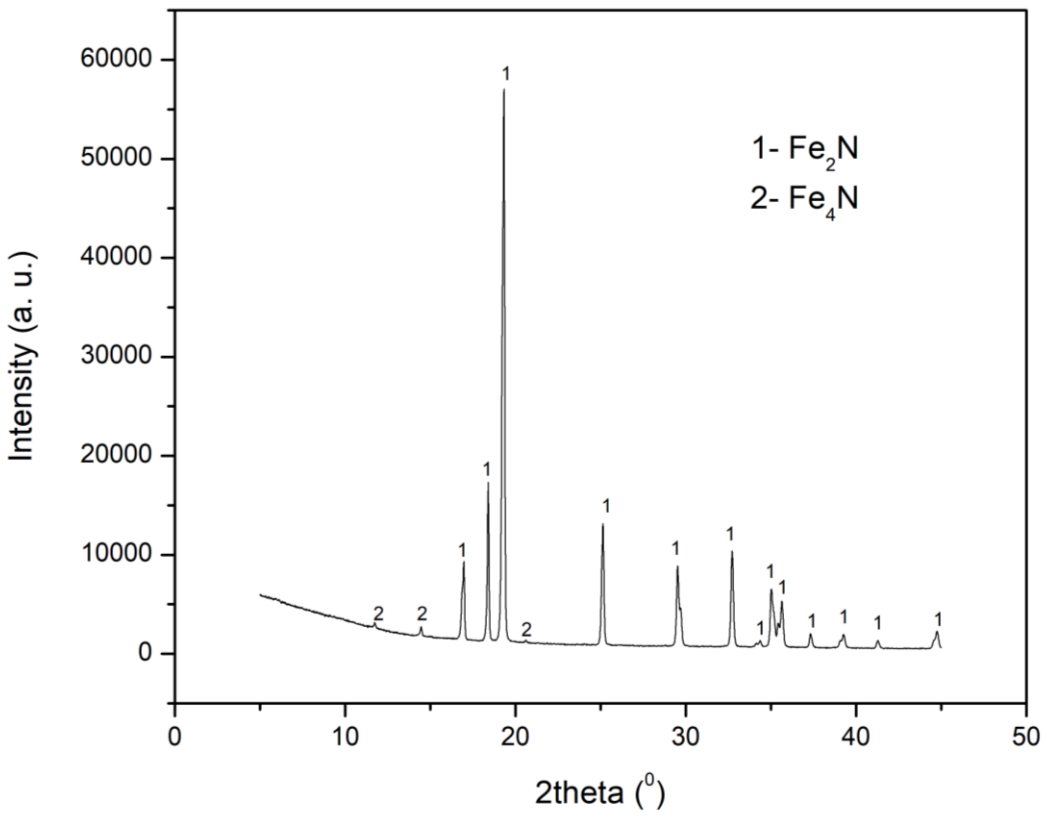

Figure 4-9 XRD pattern of Fe_2N system by solvent-deficient approach.

Figure 4-10 shows Raman spectrum of this sample. The shifts observed at 214 cm^{-1}, 274 cm^{-1}, 385 cm^{-1} and 581 cm^{-1} correspond to Fe_2N, and are in line with the XRD result [90, 91].

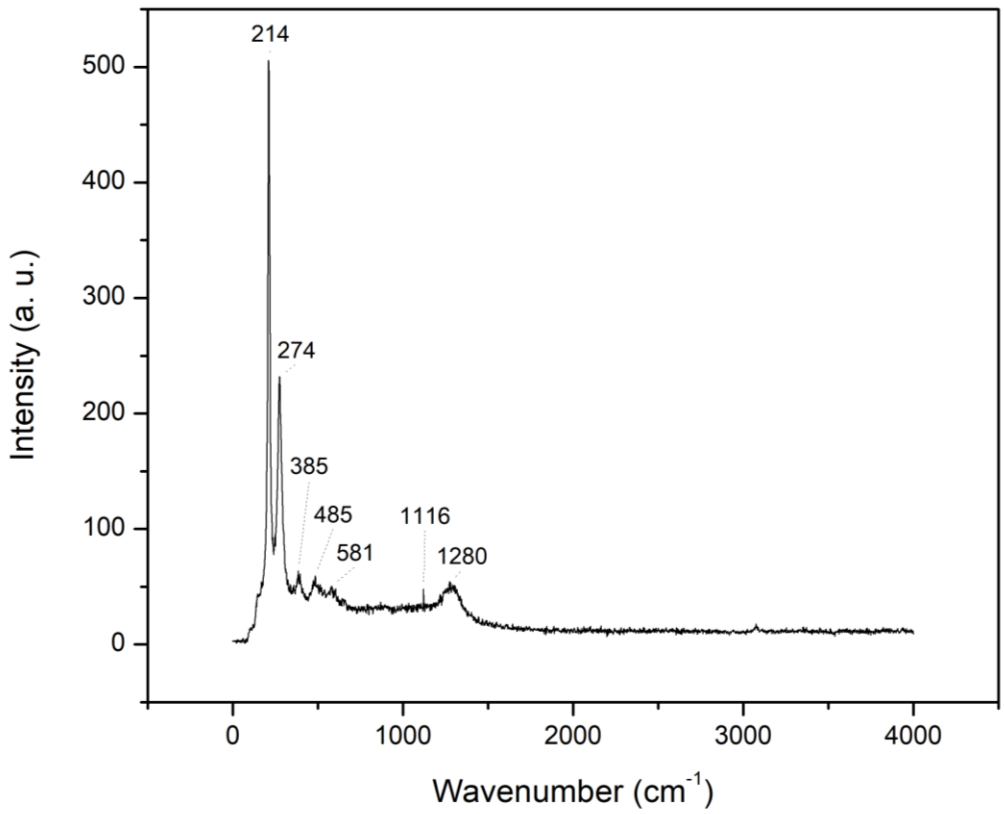

Figure 4-10 Raman spectrum of reference material system Fe_2N- solvent-deficient method ammonolyzed at $900°C$ for 2 hours.

4.2.2. Experiment 2 a: Precursor 2 Ammonolyzed at $900°C$ for 2h

This approach seems promising in order to obtain nitrides, as the XRD pattern in Figure 4-11 confirms formation of Fe_2N. However, an oxide phase i.e., magnetite is also present.

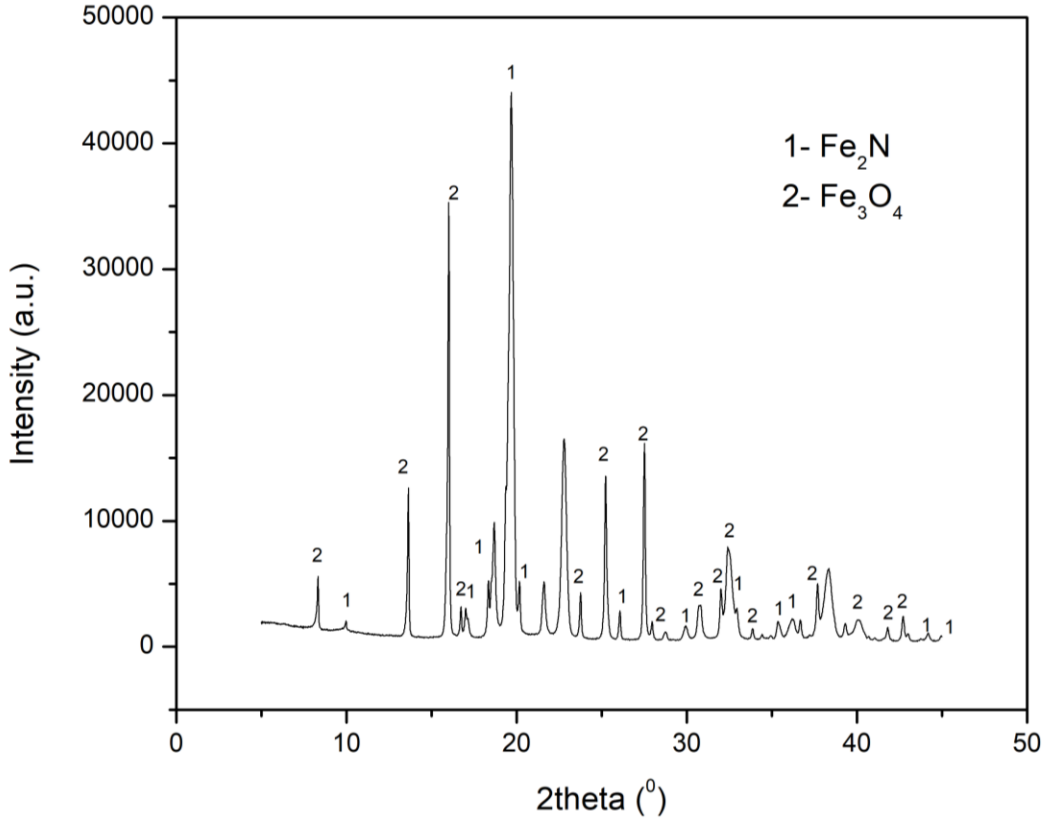

Figure 4-11 XRD Pattern of reference material system Fe_2N – Solvent-deficient method ammonolyzed at $900°C$ for 2 hours.

The Raman spectrum of this sample (Figure 4-12) indicates strong signals at 503 cm^{-1} and 672 cm^{-1}, which are characteristic of $\gamma - Fe_3O_4$ [92], and the shoulder below 503 cm-1 is likely due to iron nitride.

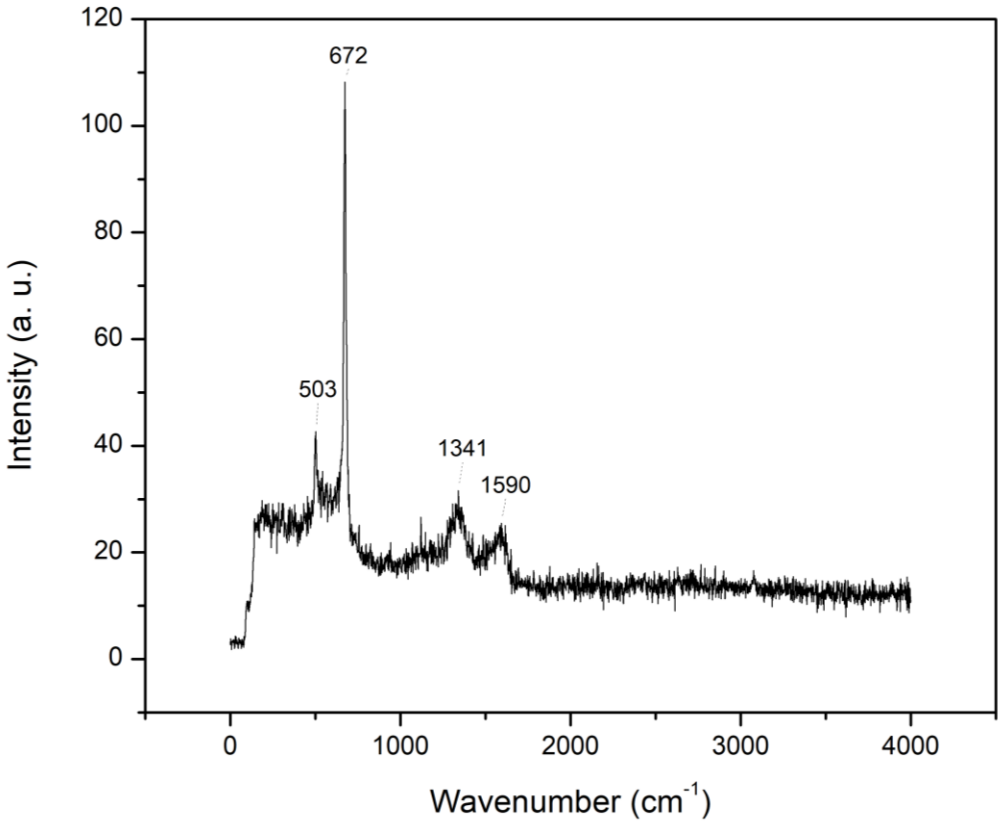

Figure 4-12 Raman spectrum of reference material system Fe_2N – Solvent-deficient method ammonolyzed at $900°C$ for 2 hours.

4.2.3. Experiment 2 b: Precursor 2 Ammonolyzed at $600°C$ for 2h

The XRD pattern of this sample (Figure 4-13) confirms the formation of nitride phases. There is Fe_2N present, which may also incorporate Fe_3N. There is also an indication of minute amount of secondary FeN phase as matched with the standard pattern i.e., ICSD ID 26116. As compared to the sample that was ammonolyzed at $900°C$, this sample, ammonolyzed at a lower temperature i.e., $600°C$, does not have any oxide phases. Although it still has secondary phase, but both phases are nitrogen-based.

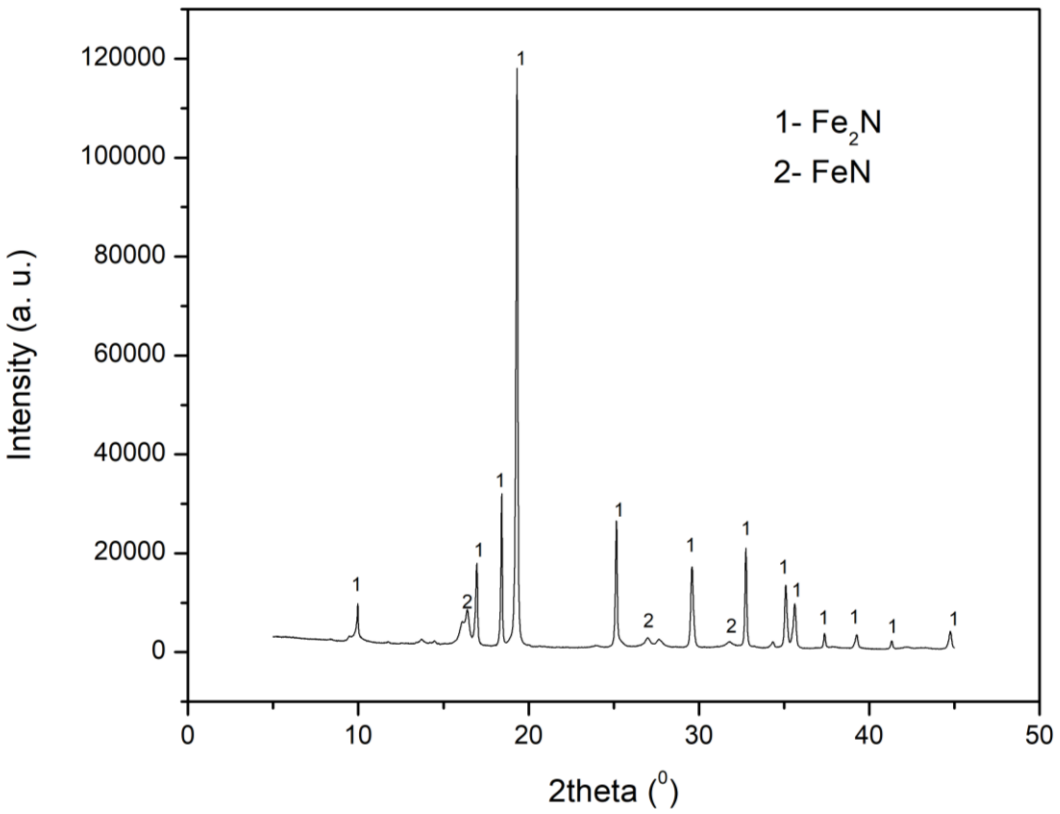

Figure 4-13 XRD Pattern of reference material system Fe_2N- hydrothermal method ammonolyzed at $600°C$ for 2 hours.

Figure 4-14 shows Raman spectrum of the sample. This sample indicated signals at 218 cm^{-1}, 290 cm^{-1}, 392 cm^{-1} due to presence of Fe_2N, along with D, G and 2D bands of carbon, that has a significant presence due to the use of glycine, which is the source of carbon present in the sample.

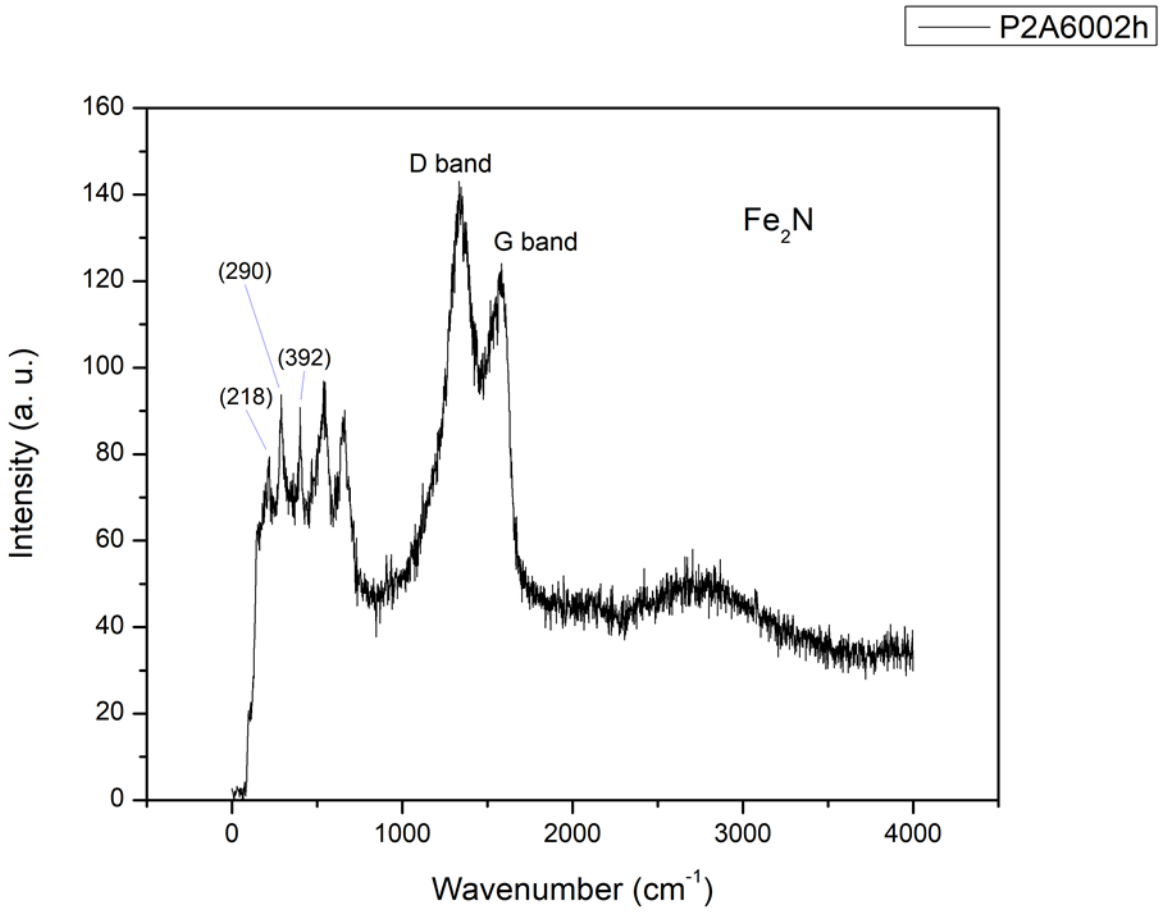

Figure 4-14 Raman spectrum of reference material system Fe_2N- hydrothermal method ammonolyzed at $600°C$ for 2 hours.

4.2.4. Experiment 3 a: Precursor 3 ammonolyzed at $900°C$ for 2h

For this sample, The XRD pattern is shown in Figure 4-15. There is a strong indication of presence of chromium nitride (CrN cubic $Fm\bar{3}m$) [93, 94]. The reflections that are identified as $Fe_{0.5}Mn_{0.2}Ni_{0.3}$ ()[93] and $Co_{0.027}Fe_{0.283}Ni_{0.689}$ according to reference pattern from crystallography open database entry 9000089 [95]. Indicate a high entropy alloy phase. This reflection pattern is also very similar to the high entropy cantor alloy, and its formation can be concluded [96]. However, the system has a secondary nitride phase as well.

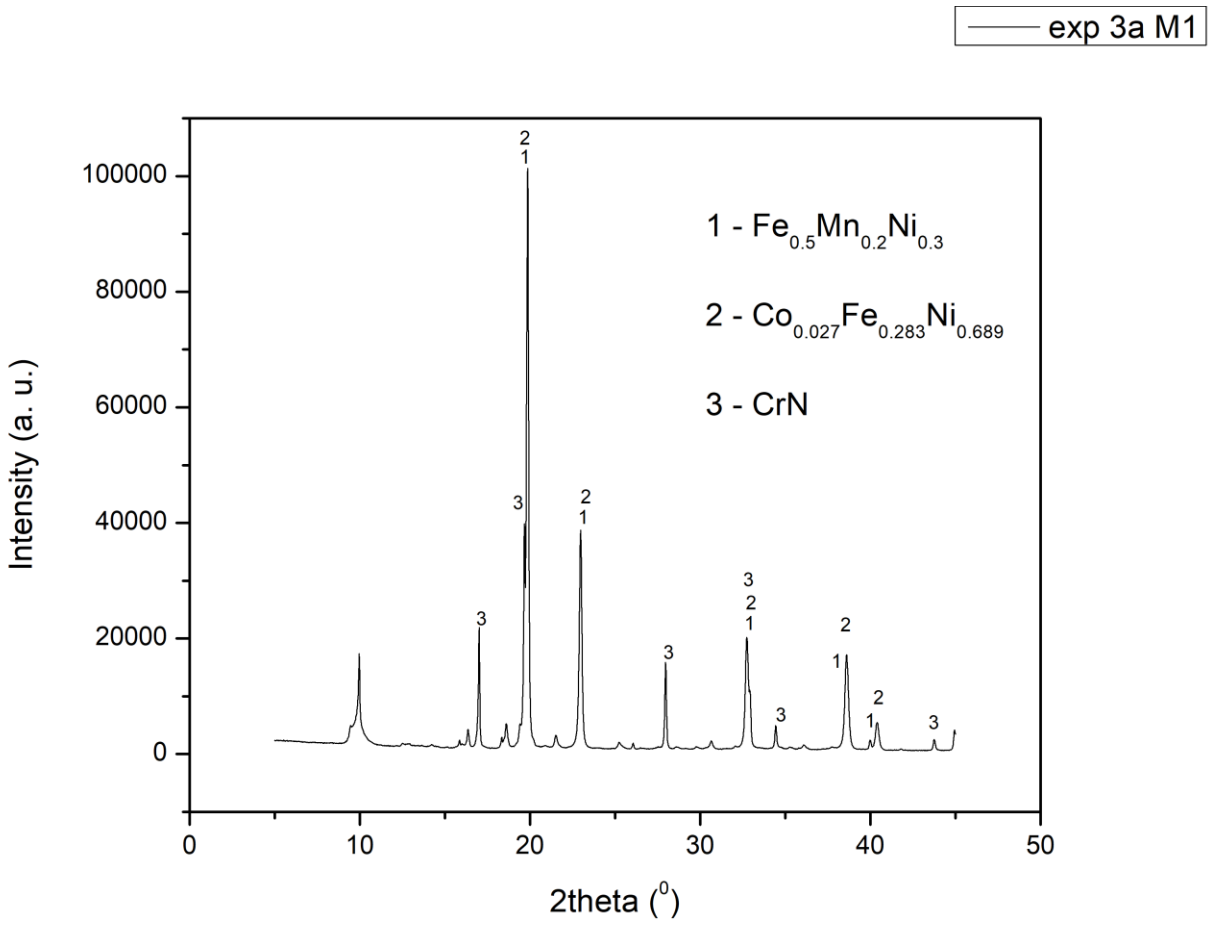

Figure 4-15 XRD pattern of material system $(Co_{0.2}Cr_{0.2}Fe_{0.2}Mn_{0.2}Ni_{0.2})_2N$ synthesized by hydrothermal method, ammonolyzed at $900°C$ for 2 hours.

The Raman spectrum for this sample (Figure 4-16) is quite similar to figure (4-12), it strongly indicates the presence of carbon, and the spectrum between 200 cm^{-1} and 800 cm^{-1} indicates CrN and Fe_2N [90, 97, 98].

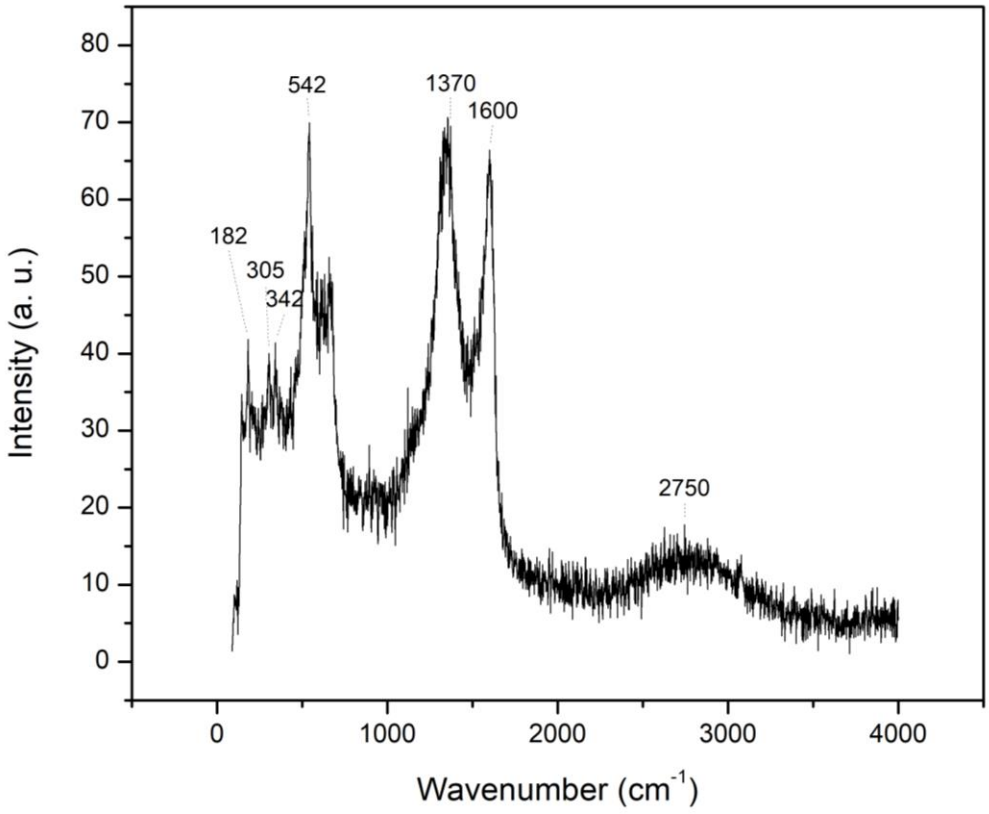

Figure 4-16 Raman spectrum of material system $(Co_{0.2}Cr_{0.2}Fe_{0.2}Mn_{0.2}Ni_{0.2})_2N$ synthesized by hydrothermal method, ammonolyzed at $900°C$ for 2 hours.

4.2.5. Experiment 3 b: Precursor 3 ammonolyzed $500°C$ for 2h

The phase composition of this sample seems to be similar to the one ammonolyzed at $900°C$, but the difference is that the secondary nitride phase is more prominent, as seen in the diffraction pattern (Figure 4-17). This shows that this approach is promising for the formation of high-entropy nitrides, however, temperature $900°C$ is too high for the high-entropy nitride phase to be stable. At $500°C$ still, the primary phase is the possibly high-entropy metallic alloy.

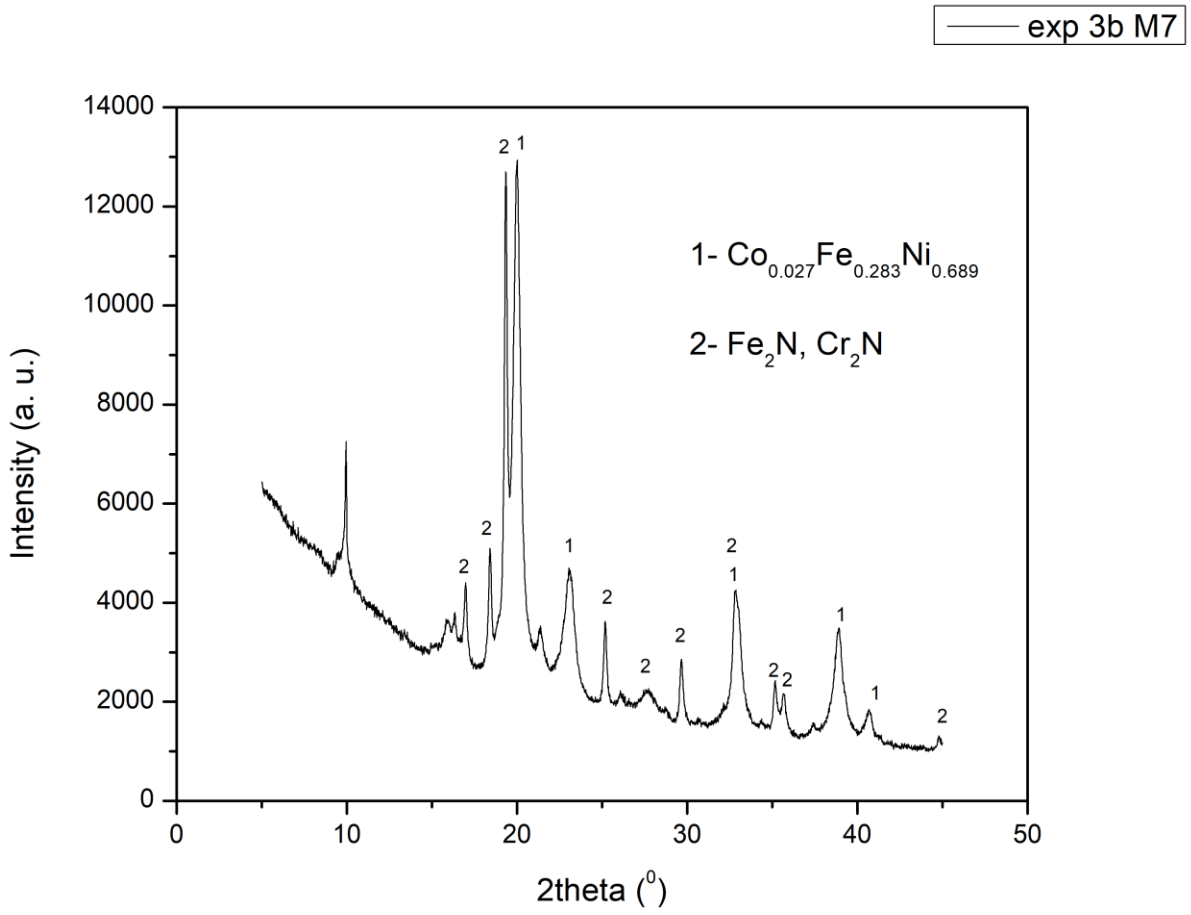

Figure 4-17 XRD pattern of material system $(Co_{0.2}Cr_{0.2}Fe_{0.2}Mn_{0.2}Ni_{0.2})_2N$ synthesized by hydrothermal method, ammonolyzed at $500°C$ for 2 hours.

Unfortunately for this sample, good quality Raman spectrum was not obtained. However, as seen in the Figure 4-18 , the small shifts observed are similar to the ones observed in previous spectra for metal nitrides.

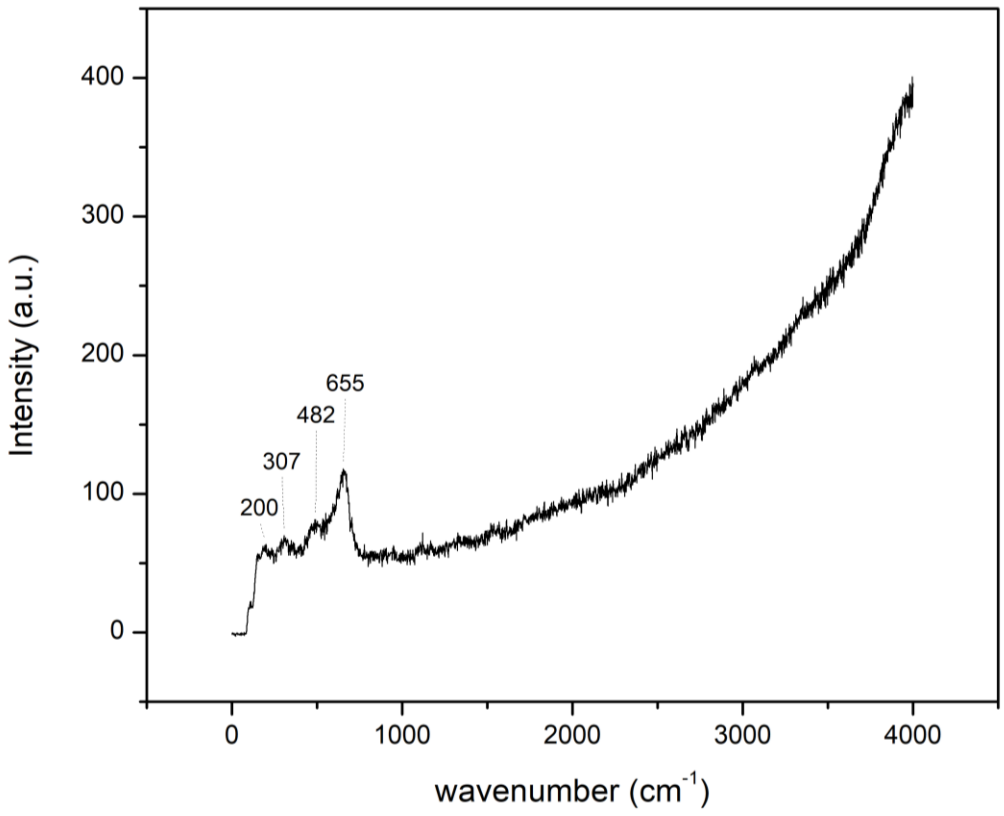

Figure 4-18 Raman spectrum of material system $(Co_{0.2}Cr_{0.2}Fe_{0.2}Mn_{0.2}Ni_{0.2})_2N$ synthesized by hydrothermal method, ammonolyzed at $500°C$ for 2 hours.

4.2.6. Experiment 4 a: Precursor 4 ammonolyzed at $900°C$ for 2h

The XRD pattern of this sample shows indication of binary nitrides of iron and chromium as secondary minute phases (Figure 4-19). However, the primary phase is likely to be a high-entropy oxide phase, as the diffraction pattern matches quite well with spinel-type Cr_2MnO_4 belonging to space group $Fd\bar{3}m$.

The obtained product was then annealed at $1250°C$ under Argon atmosphere. The Figure 4-20 shows XRD pattern of the resultant product. It shows that most of the oxide phase has been reduced, and a medium or high-entropy alloy seems to be the primary phase. The assignment of the peaks in both diffraction patterns is based on references [87, 94, 99].

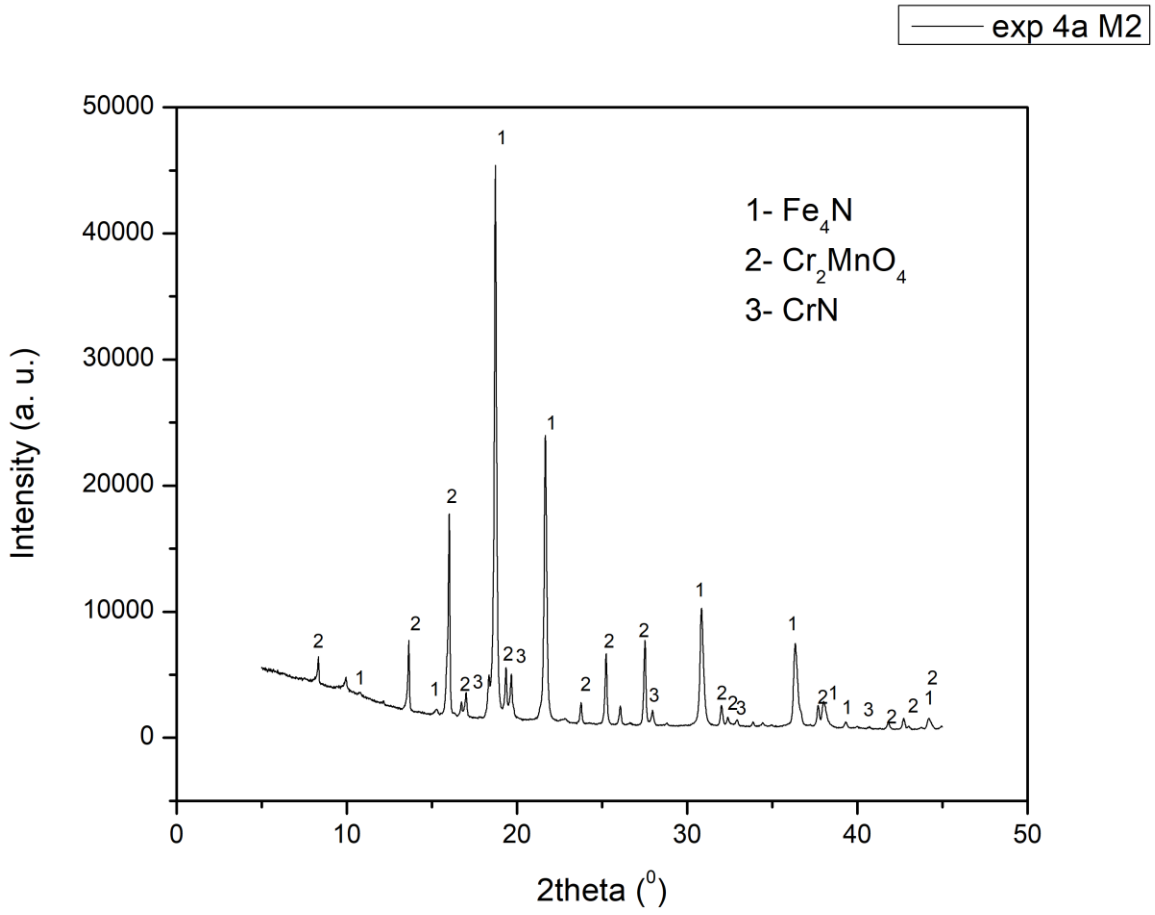

Figure 4-19 XRD pattern of material system $(Co_{0.2}Cr_{0.2}Fe_{0.2}Mn_{0.2}Ni_{0.2})_2N$ synthesized by solvent-deficient method, ammonolyzed at $900°C$ for 2 hours.

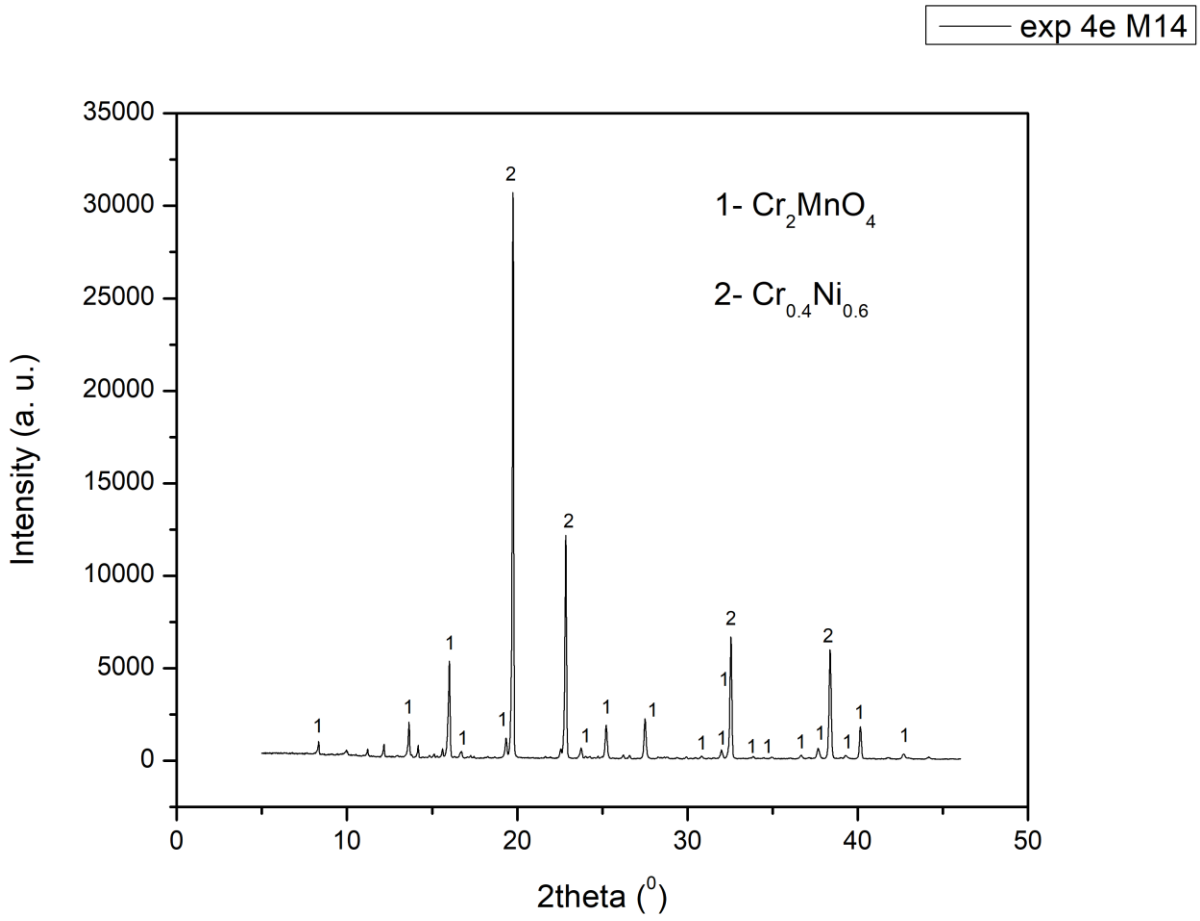

Figure 4-20 XRD pattern of material system $(Co_{0.2}Cr_{0.2}Fe_{0.2}Mn_{0.2}Ni_{0.2})_2N$ *synthesized by solvent-deficient method, ammonolyzed at* $900°C$ *for 2 hours, Annealed in Argon at* $1250°C$ *for 3 hours.*

The Figure 4-21 shows Raman spectra for the ammonolyzed sample before and after annealing, and the shifts are observed at exactly the same position. The peak positions 188 cm^{-1}, 503 cm^{-1}, and 672 cm^{-1} which has been reported to be typical for spinel oxides [100, 101]. This is in agreement with the XRD data.

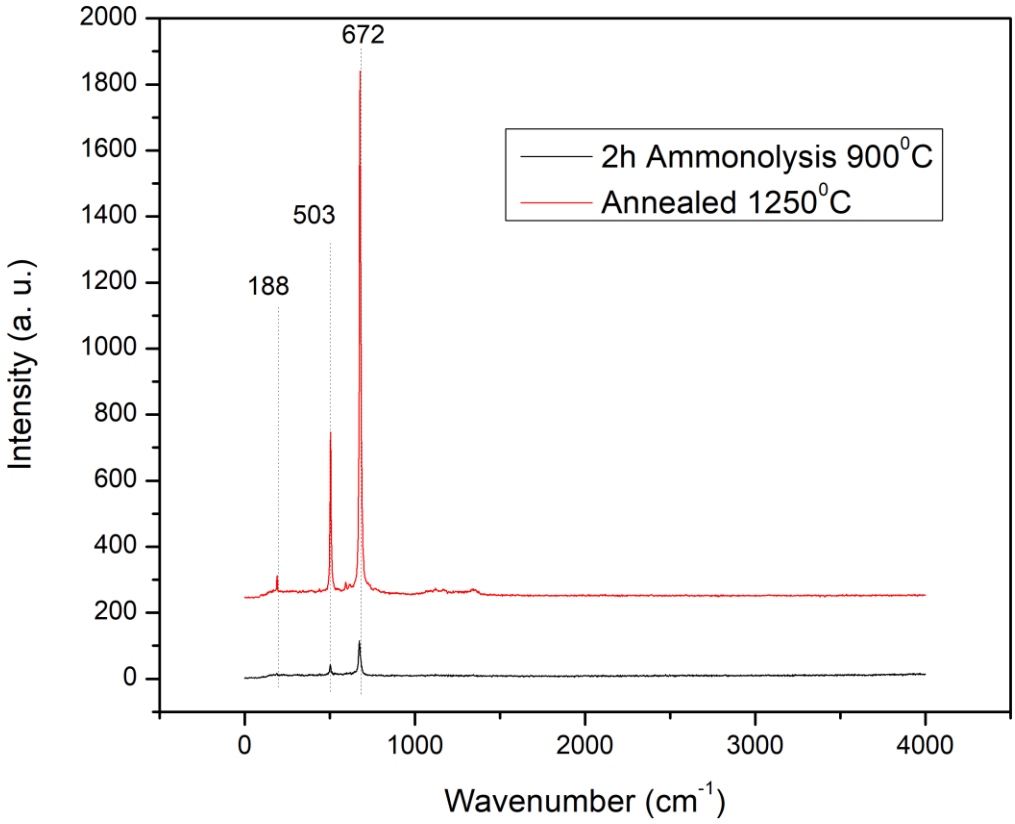

Figure 4-21 XRD pattern of material system $(Co_{0.2}Cr_{0.2}Fe_{0.2}Mn_{0.2}Ni_{0.2})_2N$ synthesized by solvent-deficient method.

4.2.7. Experiment 4 b: Precursor 4 ammonolyzed at $500°C$ for 2h

The XRD pattern of this sample in Figure 4-22 shows biphasic system. One phase is likely to be a high-entropy oxide, and the other more abundant phase is possibly high-entropy cantor alloy, as the pattern for the alloy is similar to the Cantor alloy, as well as the standard patterns for Cr, Co, Mn, Fe, and Ni in ICSD. The analysis is based on the references [96, 99, 102, 103]

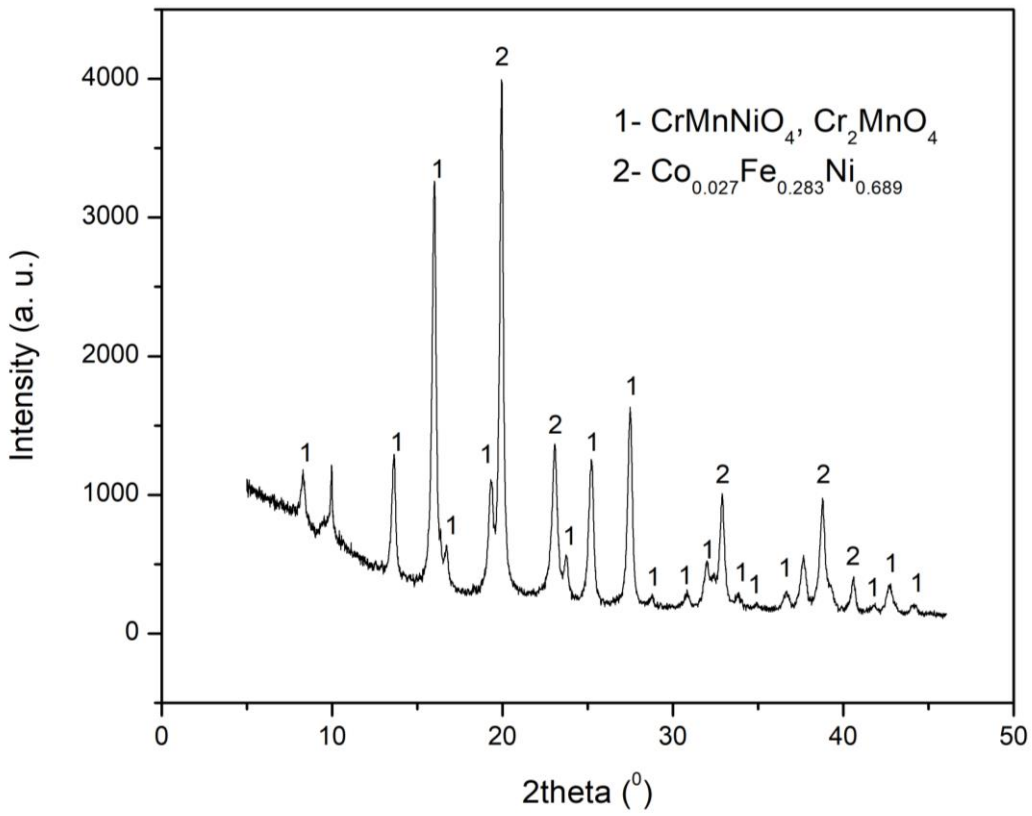

Figure 4-22 XRD pattern of material system $(Co_{0.2}Cr_{0.2}Fe_{0.2}Mn_{0.2}Ni_{0.2})_2N$ *synthesized by solvent-deficient method, ammonolyzed at* $500°C$.

4.2.8. Experiment 4 c: Precursor 4 ammonolyzed at $500°C$ for 5h

The multicomponent precursor prepared by solvent deficient method was also ammonolyzed at $500°C$ for 5 hours. The resultant product Figure 4-23 had almost exactly the same XRD pattern as Figure 4-22 for the sample ammonolyzed at $500°C$ for 2 hours, and there is no indication on Nitrogen containing phase.

4.2.9. Experiment 4 d: Precursor 4 ammonolyzed at $500°C$ for 2h – Annealed $1250°C$ for 3h in Argon

The sample that was obtained after ammonolysis at $500°C$ for 2 hours was also thermally treated at $1250°C$ under Argon flow for 3 hours in order to obtain a single-phase high-entropy alloy. However, there was still some oxide phase left that had not been completely reduced. However, thermal treatment resulted in significant improvement of crystallinity and reduction of the oxide phase, as can be observed in Figure 4-23 .

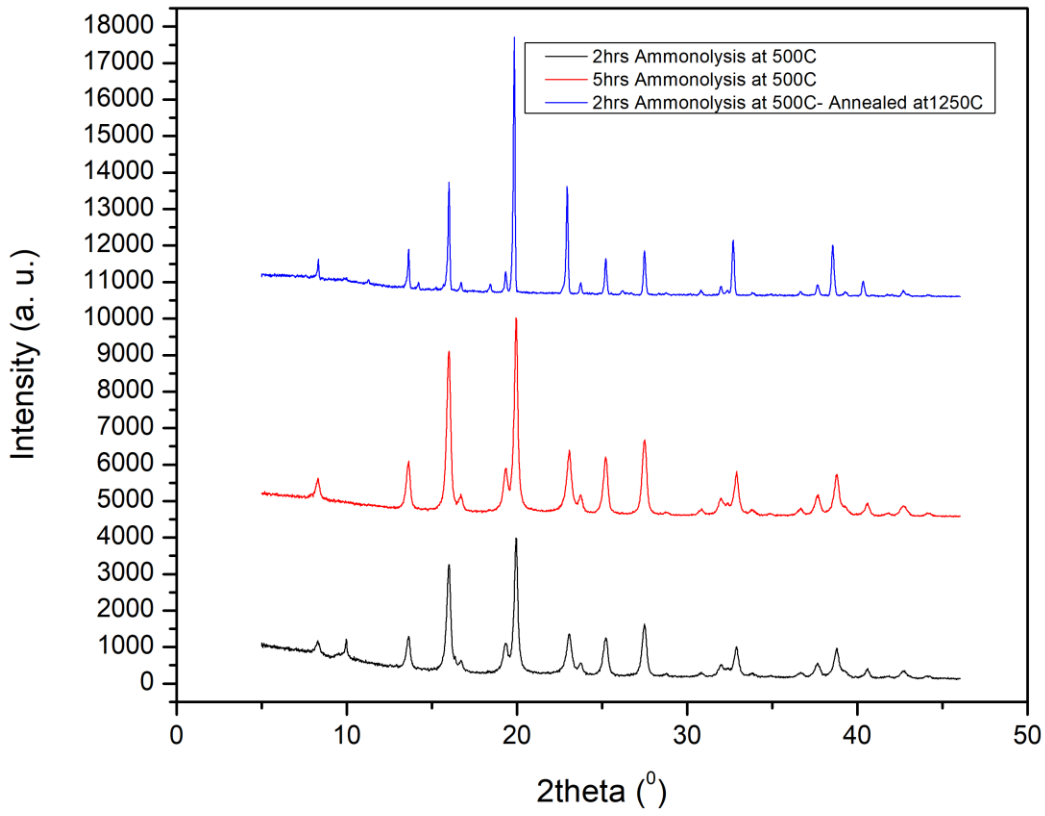

Figure 4-23 XRD pattern of material system $(Co_{0.2}Cr_{0.2}Fe_{0.2}Mn_{0.2}Ni_{0.2})_2N$ synthesized by solvent-deficient method.

The Raman spectra of these samples below (Figure 4-24) also indicate the shifts, at similar positions as in Figure 4-21 due to spinel oxides.

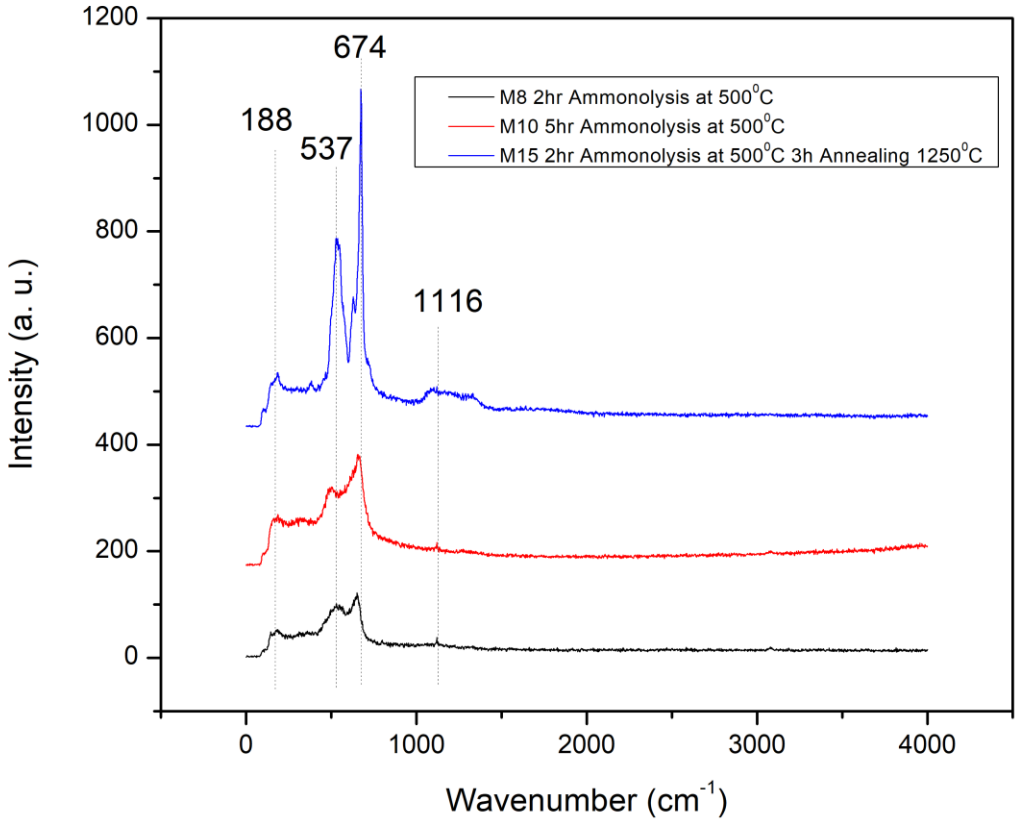

Figure 4-24 Raman spectra of material system $(Co_{0.2}Cr_{0.2}Fe_{0.2}Mn_{0.2}Ni_{0.2})_2N$ synthesized by solvent-deficient method.

4.2.10. Experiment 4 e: Precursor 4 ammonolyzed at $200°C$ for 5h

The 5-component solvent-deficient precursor was also ammonolyzed at $200°C$ for 5 hours, however the ceramization probably did not occur, as indicated by TGA results. The XRD pattern didn't give any useful information, as the sample has very poor crystallinity Figure 4-25 .

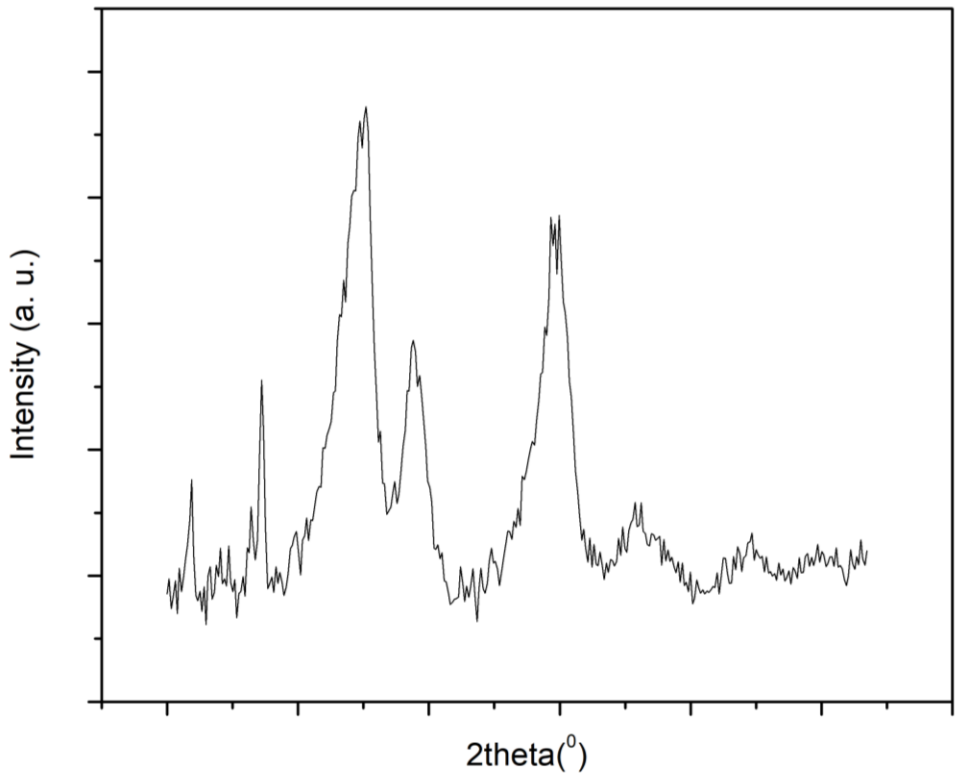

Figure 4-25 XRD pattern of material system $(Co_{0.2}Cr_{0.2}Fe_{0.2}Mn_{0.2}Ni_{0.2})_2N$ synthesized by solvent-deficient method, ammonolyzed at $200°C$ for 5 hours.

5. Conclusion and Outlook

In this work, an attempt to synthesize a high-entropy nitride system consisting of five transition metals has been done, using urea and glycine assisted hydrothermal synthesis, and solvent-deficient method. Both these routes are rather new and innovative approaches for synthesis of high-entropy materials and show potential as routes for convenient accessibility of high-entropy materials. A brief overview of the experimental aspect of this work has been presented in Table 5-1.

Starting Material	Ammonolysis Temp (°C), Time (h)	Thermal Annealing in Argon Temp (°C), Time (h)	Phases
Precursor 1 (1-component solvent-deficient synthesis)	$900°C$, 2h		Fe_2N (P -3 m 1), Fe_4N
Precursor 2 (1-component hydrothermal synthesis)	$900°C$, 2h		Fe_2N, Fe_3O_4
	$600°C$, 2h		Fe_2N, FeN
Precursor 3 (5-component hydrothermal synthesis)	$900°C$, 2h		$FeMnNiCoCr$ HEA, CrN
	$500°C$, 2h		Fe_2N, Cr_2N, FCC Cantor HEA
Precursor 4 (5-component solvent-deficient synthesis)	$900°C$, 2h	$1250°C$, 3h	Before thermal annealing: Fe_4N, CrN, HE Oxide
			After thermal annealing: Spinel HE oxide, FCC Cantor HEA
	$500°C$, 2h	$1250°C$, 3h	Spinel HE Oxide, FCC Cantor HEA
	$500°C$, 5h		Spinel HE Oxide, FCC Cantor HEA
	$200°C$, 5h		No ceramization

Table 5-1 Summary of experiments and resultant phases

It can be concluded from the reference system based on Fe_2N, that both the synthesis routes selected are suitable for formation of nitrogen containing compounds. Although single-phase composition was not obtained for the selected set of conditions, still there were not too many phases in the resultant products. Even though for single-component reference system, the solvent-deficient approach resulted in all nitride composition after ammonolysis at $900°C$ for 2 hours, and hydrothermal approach resulted in entirely nitride products after ammonolysis at $600°C$ for 2 hours, however, single-phase nitrides for 5-component system were not achieved under the same conditions. Ammonolysis of precursor 2 at $600°C$ for 2 hours resulted in coexisting FeN and Fe_2N phases. This could probably be due to the effect of crystallite size, and nitriding potential of the gas flow, as theoretical studies have pointed out that active surface area of

the crystallite undergoing phase transition is linearly proportional to nitride potential for phase transition, for both reducing and nitriding reaction [74].

Interestingly, XRD patterns provided suitable evidenced towards formation of high-entropy alloy compositions. 5-component solvent deficient precursors leaned towards high-entropy oxide formation, rather than nitride, along with significant quantity of alloy phase. Exposing these products to further higher temperature ($1250°C$) under inert atmosphere for 3 hours resulted in significant reduction of the oxide phase, and formation of high-entropy alloy as the primary phase. It can be concluded that slightly higher temperature or longer annealing times can yield phase-pure high-entropy alloy. It had already been concluded in the thesis work of a senior colleague that the solvent-deficient approach is quite suitable for high-entropy oxide formation by thermal treatment in air. However, it also has strong tendency for oxide formation even in ammonia atmosphere. There was only one case where some nitride formation was observed for this precursor, and that was the ammonolysis at $900°C$ for 2 hours. Further thermal annealing of this product completely eliminated the nitride phase. The hydrothermal approach may be more promising in obtaining the high-entropy nitride, as the XRD results show no indication of presence of oxides, and relatively stronger indication of nitride-based phase.

In conclusion, both the synthesis routes investigated showed good potential for synthesis of high-entropy materials with good crystallinity. For successful synthesis of single-phase nitrides, the reaction conditions need to be further optimized. Longer hydrothermal reaction times and higher temperatures may assist in incorporation of nitrogen already in the precursor phase. Furthermore, more advanced characterization techniques should be used to gather more information about the phases formed and the exact reaction mechanisms involved, in order to better optimize the process to increase the possibility of formation of single-phase high-entropy materials.

6. References

[1] Y. Zhang, "History of High-Entropy Materials," in *High-Entropy Materials: A Brief Introduction*, Y. Zhang, Ed., ed Singapore: Springer Singapore, 2019, pp. 1-33.

[2] D. Bérardan, S. Franger, A. K. Meena, and N. Dragoe, "Room temperature lithium superionic conductivity in high entropy oxides," *Journal of Materials Chemistry A,* vol. 4, pp. 9536-9541, 2016.

[3] H. Xiang, Y. Xing, F.-z. Dai, H. Wang, L. Su, L. Miao*, et al.*, "High-entropy ceramics: Present status, challenges, and a look forward," *Journal of Advanced Ceramics,* vol. 10, pp. 385-441, 2021/06/01 2021.

[4] D. Moskovskikh, S. Vorotilo, V. Buinevich, A. Sedegov, K. Kuskov, A. Khort*, et al.*, "Extremely hard and tough high entropy nitride ceramics," *Scientific Reports,* vol. 10, p. 19874, 2020/11/16 2020.

[5] J.-W. Yeh, A.-C. Yeh, and S.-Y. Chang, "Potential Applications and Prospects," in *High-Entropy Alloys: Fundamentals and Applications*, M. C. Gao, J.-W. Yeh, P. K. Liaw, and Y. Zhang, Eds., ed Cham: Springer International Publishing, 2016, pp. 493-512.

[6] R.-Z. Zhang, F. Gucci, H. Zhu, K. Chen, and M. J. Reece, "Data-Driven Design of Ecofriendly Thermoelectric High-Entropy Sulfides," *Inorganic Chemistry,* vol. 57, pp. 13027-13033, 2018/10/15 2018.

[7] B. Cantor, "Multicomponent high-entropy Cantor alloys," *Progress in Materials Science,* vol. 120, p. 100754, 2021/07/01/ 2021.

[8] Z. Grzesik, G. Smoła, M. Miszczak, M. Stygar, J. Dąbrowa, M. Zajusz*, et al.*, "Defect structure and transport properties of (Co,Cr,Fe,Mn,Ni)3O4 spinel-structured high entropy oxide," *Journal of the European Ceramic Society,* vol. 40, pp. 835-839, 2020/03/01/ 2020.

[9] E. P. George, D. Raabe, and R. O. Ritchie, "High-entropy alloys," *Nature Reviews Materials,* vol. 4, pp. 515-534, 2019/08/01 2019.

[10] J. W. Yeh, S. K. Chen, S. J. Lin, J. Y. Gan, T. S. Chin, T. T. Shun*, et al.*, "Nanostructured High-Entropy Alloys with Multiple Principal Elements: Novel Alloy Design Concepts and Outcomes," *Advanced Engineering Materials,* vol. 6, pp. 299-303, 2004/05/01 2004.

[11] Y. Zhang, *High-Entropy Materials: A Brief Introduction*, 2019.

[12] U. Mizutani, "Hume-Rothery rules for structurally complex alloy phases," *MRS Bulletin,* vol. 37, pp. 169-169, 2012.

[13] T. E. Whitfield, E. J. Pickering, L. R. Owen, O. N. Senkov, D. B. Miracle, H. J. Stone*, et al.*, "An assessment of the thermal stability of refractory high entropy superalloys," *Journal of Alloys and Compounds,* vol. 857, p. 157583, 2021/03/15/ 2021.

[14] C. Zhang and M. C. Gao, "CALPHAD Modeling of High-Entropy Alloys," in *High-Entropy Alloys: Fundamentals and Applications*, M. C. Gao, J.-W. Yeh, P. K. Liaw, and Y. Zhang, Eds., ed Cham: Springer International Publishing, 2016, pp. 399-444.

[15] H. Diao, X. Xie, F. Sun, K. A. Dahmen, and P. K. Liaw, "Mechanical Properties of High-Entropy Alloys," in *High-Entropy Alloys: Fundamentals and Applications*, M. C. Gao, J.-W. Yeh, P. K. Liaw, and Y. Zhang, Eds., ed Cham: Springer International Publishing, 2016, pp. 181-236.

[16] Y. Zhang, "Materials Design of High-Entropy Materials," in *High-Entropy Materials: A Brief Introduction*, Y. Zhang, Ed., ed Singapore: Springer Singapore, 2019, pp. 35-63.

[17] K. Y. Tsai, M. H. Tsai, and J. W. Yeh, "Sluggish diffusion in Co–Cr–Fe–Mn–Ni high-entropy alloys," *Acta Materialia,* vol. 61, pp. 4887-4897, 2013.

[18] H.-P. Chou, Y.-S. Chang, S.-K. Chen, and J.-W. Yeh, "Microstructure, thermophysical and electrical properties in AlxCoCrFeNi (0≤x≤2) high-entropy alloys," *Materials Science and Engineering: B,* vol. 163, pp. 184-189, 2009/07/25/ 2009.

[19] S. Ranganathan, "Alloyed pleasures: Multimetallic cocktails," 2003.

[20] C.-J. Tong, Y.-L. Chen, J.-W. Yeh, S.-J. Lin, S.-K. Chen, T.-T. Shun*, et al.*, "Microstructure characterization of AlxCoCrCuFeNi high-entropy alloy system with multiprincipal elements," *Metallurgical and Materials Transactions A,* vol. 36, pp. 881-893, 2005/04/01 2005.
[21] B. Cantor, "Multicomponent and High Entropy Alloys," *Entropy,* vol. 16, pp. 4749-4768, 2014.
[22] F. Otto, A. Dlouhý, C. Somsen, H. Bei, G. Eggeler, and E. P. George, "The influences of temperature and microstructure on the tensile properties of a CoCrFeMnNi high-entropy alloy," *Acta Materialia,* vol. 61, pp. 5743-5755, 2013/09/01/ 2013.
[23] O. N. Senkov, G. B. Wilks, D. B. Miracle, C. P. Chuang, and P. K. Liaw, "Refractory high-entropy alloys," *Intermetallics,* vol. 18, pp. 1758-1765, 2010/09/01/ 2010.
[24] O. N. Senkov and S. L. Semiatin, "Microstructure and properties of a refractory high-entropy alloy after cold working," *Journal of Alloys and Compounds,* vol. 649, pp. 1110-1123, 2015/11/15/ 2015.
[25] G. Dirras, L. Lilensten, P. Djemia, M. Laurent-Brocq, D. Tingaud, J. P. Couzinié*, et al.*, "Elastic and plastic properties of as-cast equimolar TiHfZrTaNb high-entropy alloy," *Materials Science and Engineering: A,* vol. 654, pp. 30-38, 2016/01/27/ 2016.
[26] M.-H. Tsai, "Three Strategies for the Design of Advanced High-Entropy Alloys," *Entropy,* vol. 18, 2016.
[27] O. Senkov, J. Scott, S. Senkova, D. Miracle, and C. Woodward, "Microstructure and Room Temperature Properties of a High-Entropy TaNbHfZrTi Alloy (Preprint)," *Journal of Alloys and Compounds,* vol. 509, pp. 6043-8, 05/19 2011.
[28] C.-S. Chen, C.-C. Yang, H.-Y. Chai, J.-W. Yeh, and L. Chou, "Novel cermet material of WC/multi-element alloy," *International Journal of Refractory Metals and Hard Materials,* vol. 43, pp. 200–204, 03/01 2014.
[29] T. Egami, W. Guo, P. D. Rack, and T. Nagase, "Irradiation Resistance of Multicomponent Alloys," *Metallurgical and Materials Transactions A,* vol. 45, pp. 180-183, 2014/01/01 2014.
[30] T. Nagase, S. Anada, P. D. Rack, J. H. Noh, H. Yasuda, H. Mori*, et al.*, "MeV electron-irradiation-induced structural change in the bcc phase of Zr–Hf–Nb alloy with an approximately equiatomic ratio," *Intermetallics,* vol. 38, pp. 70-79, 2013/07/01/ 2013.
[31] W. D. Callister and D. G. Rethwisch, *Materials Science and Engineering: An Introduction, 8th Edition*: Wiley, 2009.
[32] P. B. Vandiver, O. Soffer, B. Klima, and J. Svoboda, "The Origins of Ceramic Technology at Dolni Věstonice, Czechoslovakia," *Science,* vol. 246, pp. 1002-1008, 1989.
[33] in *Handbook of Advanced Ceramics (Second Edition)*, S. Somiya, Ed., ed Oxford: Academic Press, 2013, pp. 1213-1229.
[34] R. Falckenberg, "The Verneuil Process," in *Crystal Growth: Theory and Techniques Volume 2*, C. H. L. Goodman, Ed., ed Boston, MA: Springer US, 1978, pp. 109-184.
[35] H. Hassanin, K. Essa, A. Elshaer, M. Imbaby, H. H. El-Mongy, and T. A. El-Sayed, "Micro-fabrication of ceramics: Additive manufacturing and conventional technologies," *Journal of Advanced Ceramics,* vol. 10, pp. 1-27, 2021/02/01 2021.
[36] J. Hojo, *Materials Chemistry of Ceramics*, 2019.
[37] R.-Z. Zhang and M. J. Reece, "Review of high entropy ceramics: design, synthesis, structure and properties," *Journal of Materials Chemistry A,* vol. 7, pp. 22148-22162, 2019.
[38] P. Sarker, T. Harrington, C. Toher, C. Oses, M. Samiee, J.-P. Maria*, et al.*, "High-entropy high-hardness metal carbides discovered by entropy descriptors," *Nature Communications,* vol. 9, p. 4980, 2018/11/26 2018.
[39] R. Liu, H. Chen, K. Zhao, Y. Qin, B. Jiang, T. Zhang*, et al.*, "Entropy as a Gene-Like Performance Indicator Promoting Thermoelectric Materials," *Advanced Materials,* vol. 29, p. 1702712, 2017/10/01 2017.

[40] R. Djenadic, A. Sarkar, O. Clemens, C. Loho, M. Botros, V. S. K. Chakravadhanula*, et al.*, "Multicomponent equiatomic rare earth oxides," *Materials Research Letters,* vol. 5, pp. 102-109, 2017/03/04 2017.

[41] J. Dąbrowa, M. Stygar, A. Mikuła, A. Knapik, K. Mroczka, W. Tejchman*, et al.*, "Synthesis and microstructure of the (Co,Cr,Fe,Mn,Ni)3O4 high entropy oxide characterized by spinel structure," *Materials Letters,* vol. 216, pp. 32-36, 2018/04/01/ 2018.

[42] C. M. Rost, E. Sachet, T. Borman, A. Moballegh, E. C. Dickey, D. Hou*, et al.*, "Entropy-stabilized oxides," *Nature Communications,* vol. 6, p. 8485, 2015/09/29 2015.

[43] H. Chen, J. Fu, P. Zhang, H. Peng, C. W. Abney, K. Jie*, et al.*, "Entropy-stabilized metal oxide solid solutions as CO oxidation catalysts with high-temperature stability," *Journal of Materials Chemistry A,* vol. 6, pp. 11129-11133, 2018.

[44] A. Sarkar, L. Velasco, D. Wang, Q. Wang, G. Talasila, L. de Biasi*, et al.*, "High entropy oxides for reversible energy storage," *Nature Communications,* vol. 9, p. 3400, 2018/08/24 2018.

[45] O. F. Dippo, N. Mesgarzadeh, T. J. Harrington, G. D. Schrader, and K. S. Vecchio, "Bulk high-entropy nitrides and carbonitrides," *Scientific Reports,* vol. 10, p. 21288, 2020/12/04 2020.

[46] W. Hong, F. Chen, Q. Shen, Y.-H. Han, W. G. Fahrenholtz, and L. Zhang, "Microstructural evolution and mechanical properties of (Mg,Co,Ni,Cu,Zn)O high-entropy ceramics," *Journal of the American Ceramic Society,* vol. 102, pp. 2228-2237, 2019/04/01 2019.

[47] A. Sedegov, S. Vorotilo, V. Tsybulin, K. Kuskov, and D. Moscovskikh, "Synthesis and study of high-entropy ceramics based on the carbides of refractory metals," *IOP Conference Series: Materials Science and Engineering,* vol. 558, p. 012043, 2019/06/24 2019.

[48] T. Maiti, M. Saxena, and P. Roy, "Double perovskite (Sr2B′ B″ O6) oxides for high-temperature thermoelectric power generation—A review," *Journal of Materials Research,* vol. 34, pp. 107-125, 2019/01/01 2019.

[49] A. Sarkar, R. Djenadic, D. Wang, C. Hein, R. Kautenburger, O. Clemens*, et al.*, "Rare earth and transition metal based entropy stabilised perovskite type oxides," *Journal of the European Ceramic Society,* vol. 38, pp. 2318-2327, 2018/05/01/ 2018.

[50] A. Sarkar, C. Loho, L. Velasco, T. Thomas, S. S. Bhattacharya, H. Hahn*, et al.*, "Multicomponent equiatomic rare earth oxides with a narrow band gap and associated praseodymium multivalency," *Dalton Transactions,* vol. 46, pp. 12167-12176, 2017.

[51] R. Witte, A. Sarkar, R. Kruk, B. Eggert, R. A. Brand, H. Wende*, et al.*, "High-entropy oxides: An emerging prospect for magnetic rare-earth transition metal perovskites," *Physical Review Materials,* vol. 3, p. 034406, 03/13/ 2019.

[52] P. B. Meisenheimer, T. J. Kratofil, and J. T. Heron. (2017, 2017/10//). Giant Enhancement of Exchange Coupling in Entropy-Stabilized Oxide Heterostructures. *Scientific reports 7(1),* 13344. Available: http://europepmc.org/abstract/MED/29042610

https://doi.org/10.1038/s41598-017-13810-5

https://europepmc.org/articles/PMC5645335

https://europepmc.org/articles/PMC5645335?pdf=render

[53] J. Mittra, G. Abraham, M. Kesaria, S. Bahl, R. Singh, S. Shivaprasad*, et al.*, "Role of Substrate Temperature in the Pulsed Laser Deposition of Zirconium Oxide Thin Film," *Materials Science Forum,* vol. 710, pp. 757-761, 01/01 2012.

[54] S. J. Smith, B. Huang, S. Liu, Q. Liu, R. E. Olsen, J. Boerio-Goates*, et al.*, "Synthesis of metal oxide nanoparticles via a robust “solvent-deficient” method," *Nanoscale,* vol. 7, pp. 144-156, 2015.

[55] B. Huang, S. Smith, R. Olsen, C. Bartholomew, B. Woodfield, and J. Boerio-Goates, *Novel Mesoporous Gamma-Alumina Catalyst Supports*, 2010.

[56] S. Zeljkovic, D. Jelić, H. Maruyama, and J. Nino, "Solvent-deficient synthesis of cerium oxide: Characterization and kinetics," *Ceramics International,* vol. 45, pp. 10063-10071, 06/01 2019.
[57] K. N. Nithyayini, M. N. K. Harish, and K. L. Nagashree, "Electrochemical detection of nitrite at NiFe2O4 nanoparticles synthesised by solvent deficient method," *Electrochimica Acta,* vol. 317, pp. 701-710, 2019/09/10/ 2019.
[58] S. Zeljković, T. Ivas, H. Maruyama, and J. C. Nino, "Structural, magnetic and optical properties of BiFeO3 synthesized by the solvent-deficient method," *Ceramics International,* vol. 45, pp. 19793-19798, 2019/11/01/ 2019.
[59] R. M. Kore and B. J. Lokhande, "Hierarchical mesoporous network of amorphous α − Ni(OH)2 for high performance supercapacitor electrode material synthesized from a novel solvent deficient approach," *Electrochimica Acta,* vol. 245, pp. 780-790, 2017/08/10/ 2017.
[60] A. F. Holleman, *Lehrbuch der anorganischen Chemie*: Walter de Gruyter GmbH & Co KG, 2019.
[61] A. Ali, M. Z. Hira Zafar, I. ul Haq, A. R. Phull, J. S. Ali, and A. Hussain, "Synthesis, characterization, applications, and challenges of iron oxide nanoparticles," *Nanotechnology, science and applications,* vol. 9, p. 49, 2016.
[62] E. Ameri, M. Abdollahifar, M. Zamani, and H. Nekouei, "THE ROLE OF UREA ON THE HYDROTHERMAL SYNTHESIS OF BOEHMITE NANOARCHITECTURES," *Ceramics Silikaty,* vol. 60, 03/01 2016.
[63] J. Z. Marinho, F. C. Romeiro, S. C. S. Lemos, F. V. Motta, C. S. Riccardi, M. S. Li*, et al.*, "Urea-Based Synthesis of Zinc Oxide Nanostructures at Low Temperature," *Journal of Nanomaterials,* vol. 2012, p. 427172, 2012/05/14 2012.
[64] M. A. Salvadó, P. Pertierra, A. I. Bortun, C. Trobajo, and J. R. García, "Phosphorous Acid and Urea: Valuable Sources of Phosphorus and Nitrogen in the Hydrothermal Synthesis of Ammonium-Thorium Phosphates," *Inorganic Chemistry,* vol. 47, pp. 7207-7210, 2008/08/01 2008.
[65] H. Chen, Y. Zhao, M. Yang, J. He, P. K. Chu, J. Zhang*, et al.*, "Glycine-assisted hydrothermal synthesis of peculiar porous α-Fe2O3 nanospheres with excellent gas-sensing properties," *Analytica chimica acta,* vol. 659, pp. 266-273, 2010.
[66] J. Zhou, Z. Zhang, B. Cheng, and J. Yu, "Glycine-assisted hydrothermal synthesis and adsorption properties of crosslinked porous α-Fe2O3 nanomaterials for p-nitrophenol," *Chemical engineering journal,* vol. 211, pp. 153-160, 2012.
[67] B. C.S, D. Raja, and P. Padiyan, "Glycine assisted hydrothermal synthesis of α-Fe2O3 nanoparticles and its size dependent properties," *Chemical Physics Letters,* vol. s 610–611, pp. 103–107, 08/01 2014.
[68] D. Titus, E. J. J. Samuel, and S. M. Roopan, "Nanoparticle characterization techniques," in *Green synthesis, characterization and applications of nanoparticles*, ed: Elsevier, 2019, pp. 303-319.
[69] S. A. A. Elzwawi, "Cathodic Arc Zinc Oxide for Active Electronic Devices," 2015.
[70] S. Ebnesajjad, "Surface and material characterization techniques," in *Handbook of Adhesives and Surface Preparation*, ed: Elsevier, 2011, pp. 31-48.
[71] T. E. Acosta-Maeda, A. K. Misra, L. G. Muzangwa, G. Berlanga, D. Muchow, J. Porter*, et al.*, "Remote Raman measurements of minerals, organics, and inorganics at 430 m range," *Applied Optics,* vol. 55, pp. 10283-10289, 2016/12/20 2016.
[72] M. V. Abrashev, V. G. Ivanov, B. S. Stefanov, N. D. Todorov, J. Rosell, and V. Skumryev, "Raman spectroscopy of alpha-FeOOH (goethite) near antiferromagnetic to paramagnetic phase transition," *Journal of Applied Physics,* vol. 127, p. 205108, 2020/05/29 2020.
[73] U. Topal, H. Ozkan, and H. Sozeri, "Synthesis and characterization of nanocrystalline BaFe12O19 obtained at 850 deg C by using ammonium nitrate melt," *Journal of Magnetism and Magnetic Materials,* vol. 284, pp. 416-422, 2004.

[74] B. Wilk, R. Pelka, and W. Arabczyk, "Study of the Iron Catalyst for Ammonia Synthesis by Chemical Potential Programmed Reaction Method," *The Journal of Physical Chemistry C,* vol. 121, pp. 8548-8556, 2017/04/20 2017.

[75] M. Widenmeyer, T. C. Hansen, E. Meissner, and R. Niewa, "Formation and Decomposition of Iron Nitrides Observed by in situ Powder Neutron Diffraction and Thermal Analysis," *Zeitschrift für anorganische und allgemeine Chemie,* vol. 640, pp. 1265-1274, 2014/06/01 2014.

[76] J. Glasscock, P. Barnes, I. Plumb, and N. Savvides, "Enhancement of Photoelectrochemical Hydrogen Production from Hematite Thin Flms by the Introduction of Ti and Si," *Journal of Physical Chemistry C - J PHYS CHEM C,* vol. 111, 10/10 2007.

[77] D. L. A. de Faria, S. Venâncio Silva, and M. T. de Oliveira, "Raman microspectroscopy of some iron oxides and oxyhydroxides," *Journal of Raman Spectroscopy,* vol. 28, pp. 873-878, 1997.

[78] R. W. G. Wyckoff, "The crystal structures of some carbonates of the calcite group," *American Journal of Science,* vol. s4-50, p. 317, 1920.

[79] Q. Zhao and H. J. Kulik, "Where Does the Density Localize in the Solid State? Divergent Behavior for Hybrids and DFT+U," *Journal of Chemical Theory and Computation,* vol. 14, pp. 670-683, 2018/02/13 2018.

[80] T. Varga, L. Vásárhelyi, G. Ballai, H. Haspel, A. Oszkó, A. Kukovecz*, et al.*, "Noble-Metal-Free Iron Nitride/Nitrogen-Doped Graphene Composite for the Oxygen Reduction Reaction," *ACS Omega,* vol. 4, pp. 130-139, 01/31 2019.

[81] A. Kaniyoor and S. Ramaprabhu, "A Raman spectroscopic investigation of graphite oxide derived graphene," *AIP Advances,* vol. 2, p. 032183, 2012/09/01 2012.

[82] C.-S. Zhao, H. Li, J. Jiang, Y. He, and W. Liang, "Phase Transition and vibration properties of MnCO3 at high pressure and high-temperature by Raman spectroscopy," *High Pressure Research,* pp. 1-12, 05/19 2018.

[83] N. Sanpo, A. Ang, m. f. Hasan, J. Wang, and C. Berndt, *Phases and microstructures of solution precursor plasma sprayed cobalt ferrite splats*, 2012.

[84] H. Komura, H. Akiyama, M. Fukaya, and K. Ishikawa, "Raman scattering from phonons in MnCO3," *Journal of Raman Spectroscopy,* vol. 14, pp. 330-332, 1983/10/01 1983.

[85] S. Angel, N. Gomer, S. Sharma, and C. McKay, "Remote Raman Spectroscopy for Planetary Exploration: A Review," *Applied spectroscopy,* vol. 66, pp. 137-50, 02/01 2012.

[86] W. M. Shaheen and M. M. Selim, "Thermal Decompositions of Pure and Mixed Manganese Carbonate and Ammonium Molybdate Tetrahydrate," *Journal of Thermal Analysis and Calorimetry,* vol. 59, pp. 961-970, 2000/03/01 2000.

[87] Z. Q. Liu, A. Leineweber, E. J. Mittemeijer, K. Mitsuishi, and K. Furuya, "Electron-diffraction study on ∈-iron nitride powders with various nitrogen contents: Variation of long-range nitrogen ordering," *Journal of Materials Research,* vol. 21, pp. 2572-2581, 2006/10/01 2006.

[88] A. E. Smith, "The crystal structure of the urea–hydrocarbon complexes," *Acta Crystallographica,* vol. 5, pp. 224-235, 1952/03/01 1952.

[89] J. Burghaus, M. Wessel, A. Houben, and R. Dronskowski, "Ternary Nitride GaFe3N: An Experimental and Quantum-Theoretical Study," *Inorganic Chemistry,* vol. 49, pp. 10148-10155, 2010/11/01 2010.

[90] Y. Zhang, Y. Xie, Y. Zhou, X. Wang, and K. Pan, "Well dispersed Fe2N nanoparticles on surface of nitrogen-doped reduced graphite oxide for highly efficient electrochemical hydrogen evolution," *Journal of Materials Research,* vol. 32, pp. 1770-1776, 2017.

[91] H. Jiang, L. Huang, Y. Wei, B. Wang, H. Wu, Y. Zhang*, et al.*, "Bio-Derived Hierarchical Multicore–Shell Fe2N-Nanoparticle-Impregnated N-Doped Carbon Nanofiber Bundles: A Host Material for Lithium-/Potassium-Ion Storage," *Nano-Micro Letters,* vol. 11, 07/01 2019.

[92] L. Slavov, M. V. Abrashev, T. Merodiiska, C. Gelev, R. E. Vandenberghe, I. Markova-Deneva*, et al.*, "Raman spectroscopy investigation of magnetite nanoparticles in ferrofluids," *Journal of Magnetism and Magnetic Materials,* vol. 322, pp. 1904-1911, 2010/07/01/ 2010.

[93] A. Z. Menshikov, V. A. Kazantsev, N. N. Kuzmin, and S. K. Sidorov, "Exchange interaction and magnetic properties of iron-nickel-manganese alloys," *Journal of Magnetism and Magnetic Materials,* vol. 1, pp. 91-97, 1975/11/01/ 1975.

[94] M. Widenmeyer, E. Meissner, A. Senyshyn, and R. Niewa, "On the Formation Mechanism of Chromium Nitrides: An in situ Study," *Zeitschrift für anorganische und allgemeine Chemie,* vol. 640, pp. 2801-2808, 2014/11/01 2014.

[95] K. L. Williams, "An association of awaruite with heazlewoodite," *American Mineralogist,* vol. 45, pp. 450-453, 1960.

[96] N. Eißmann, O. Steuer, U. Gaitzsch, G. Walther, T. Weissgaerber, and B. Kieback, *Phase Analysis of Co-Cr-Fe-Mn-Ni High-Entropy Alloy and the Influence of Titanium Addition*, 2018.

[97] A. Sugumaran, Y. Purandare, A. Ehiasarian, and P. Hovsepian, "Corrosion behaviour of post-deposition polished droplets-embedded arc evaporated and droplets-free HIPIMS/DCMS coatings," *Corrosion -Houston Tx- ISSN: 0010-9312,* vol. 73, 01/09 2017.

[98] H. Jiang, L. Huang, Y. Wei, B. Wang, H. Wu, Y. Zhang*, et al.*, "Bio-Derived Hierarchical Multicore–Shell Fe2N-Nanoparticle-Impregnated N-Doped Carbon Nanofiber Bundles: A Host Material for Lithium-/Potassium-Ion Storage," *Nano-Micro Letters,* vol. 11, p. 56, 2019/07/15 2019.

[99] P. M. Raccah, R. J. Bouchard, and A. Wold, "Crystallographic Study of Chromium Spinels," *Journal of Applied Physics,* vol. 37, pp. 1436-1437, 1966/03/01 1966.

[100] P. R. Kumar, Y. H. Jung, K. K. Bharathi, C. H. Lim, and D. K. Kim, "High capacity and low cost spinel Fe3O4 for the Na-ion battery negative electrode materials," *Electrochimica Acta,* vol. 146, pp. 503-510, 2014/11/10/ 2014.

[101] A. Diallo, A. C. Beye, T. B. Doyle, E. Park, and M. Maaza, "Green synthesis of Co3O4 nanoparticles via Aspalathus linearis: Physical properties," *Green Chemistry Letters and Reviews,* vol. 8, pp. 30-36, 2015/10/02 2015.

[102] E. Owen and D. Jones, "Effect of Grain Size on the Crystal Structure of Cobalt," *Proceedings of the Physical Society. Section B,* vol. 67, p. 456, 12/18 2002.

[103] N. Renault, N. Baffier, and M. Huber, "Distribution cationique et distorsion cristalline dans les manganites spinelles NiCrxMn2−xO4," *Journal of Solid State Chemistry,* vol. 5, pp. 250-254, 1972/09/01/ 1972.

UNIVERSITÉ CATHOLIQUE DE LOUVAIN
École polytechnique de Louvain
Rue Archimède, 1 bte L6.11.01, 1348 Louvain-la-Neuve, Belgique | **www.uclouvain.be/epl**